

# A diamond-confined open microcavity featuring a high quality-factor and a small mode-volume

Cite as: J. Appl. Phys. **131**, 113102 (2022); <https://doi.org/10.1063/5.0081577>

Submitted: 09 December 2021 • Accepted: 02 March 2022 • Published Online: 21 March 2022

 Sigurd Flågan,  Daniel Riedel,  Alisa Javadi, et al.

## COLLECTIONS

 This paper was selected as an Editor's Pick



View Online



Export Citation



CrossMark

## ARTICLES YOU MAY BE INTERESTED IN

[Progress and perspective in mechanically robust carbon aerogels](#)

Journal of Applied Physics **131**, 110904 (2022); <https://doi.org/10.1063/5.0084458>

[Building on excellence and reputation, a more inclusive Journal of Applied Physics evolves](#)

Journal of Applied Physics **131**, 110401 (2022); <https://doi.org/10.1063/5.0088430>

[A direct approach to calculate the temperature dependence of the electronic relaxation time in 2D semiconductors from Boltzmann transport theory](#)

Journal of Applied Physics **131**, 115704 (2022); <https://doi.org/10.1063/5.0080938>

## Lock-in Amplifiers up to 600 MHz



Zurich  
Instruments




# A diamond-confined open microcavity featuring a high quality-factor and a small mode-volume

Cite as: J. Appl. Phys. **131**, 113102 (2022); doi: [10.1063/5.0081577](https://doi.org/10.1063/5.0081577)

Submitted: 9 December 2021 · Accepted: 2 March 2022 ·

Published Online: 21 March 2022



Sigurd Flågan,<sup>a)</sup>  Daniel Riedel,<sup>b)</sup>  Alisa Javadi,  Tomasz Jakubczyk,<sup>c)</sup>  Patrick Maletinsky,   
and Richard J. Warburton 

## AFFILIATIONS

Department of Physics, University of Basel, Klingelbergstrasse 82, Basel CH-4056, Switzerland

<sup>a)</sup>Author to whom correspondence should be addressed: [sigurd.flagan@unibas.ch](mailto:sigurd.flagan@unibas.ch)

<sup>b)</sup>Current address: E. L. Ginzton Laboratory, Stanford University, Stanford, CA 94305, USA.

<sup>c)</sup>Current address: Faculty of Physics, University of Warsaw, 02-093 Warsaw, Poland.

## ABSTRACT

With a highly coherent, optically addressable electron spin, the nitrogen-vacancy (NV) center in diamond is a promising candidate for a node in a quantum network. A resonant microcavity can boost the flux of coherent photons emerging from single NV centers. Here, we present an open Fabry-Pérot microcavity geometry containing a single-crystal diamond membrane, which operates in a regime where the vacuum electric field is strongly confined to the diamond membrane. There is a field anti-node at the diamond-air interface. Despite the presence of surface losses, a finesse of  $\mathcal{F} = 11\,500$  was observed. The quality ( $Q$ ) factor for the lowest mode number is 120 000; the mode volume  $V$  is estimated to be  $3.9\lambda_0^3$ , where  $\lambda_0$  is the free-space wavelength. We investigate the interplay between different loss mechanisms and the impact these loss channels have on the performance of the cavity. This analysis suggests that the surface waviness (roughness with a spatial frequency comparable to that of the microcavity mode) is the mechanism preventing the  $Q/V$  ratio from reaching even higher values. Finally, we apply the extracted cavity parameters to the NV center and calculate a predicted Purcell factor exceeding 150.

© 2022 Author(s). All article content, except where otherwise noted, is licensed under a Creative Commons Attribution (CC BY) license (<http://creativecommons.org/licenses/by/4.0/>). <https://doi.org/10.1063/5.0081577>

## I. INTRODUCTION

The development of an efficient interface between stationary and flying qubits<sup>1,2</sup> is an essential step toward the realization of large-scale distributed quantum networks<sup>3</sup> and the quantum internet.<sup>4,5</sup> In such a network, quantum nodes with the ability to store and process quantum information are interconnected via quantum channels in order to distribute quantum information and entanglement across the network.<sup>6</sup> These network nodes require high-fidelity processing of quantum information combined with a long-lived quantum memory.<sup>7,8</sup> Long-lived, optically addressable spins in the solid-state have emerged as promising candidates.<sup>1,2,9</sup> Owing to its highly coherent,<sup>10,11</sup> optically addressable electron spin<sup>12–14</sup> and the possibility of coherent couplings to nearby nuclear spins,<sup>15–19</sup> the negatively charged nitrogen-vacancy (NV) center in diamond is a promising candidate as a stationary qubit in a quantum network.<sup>20–22</sup> However, the scalability is limited by the modest entanglement rates, in turn limited by the small flux of coherent photons.<sup>23</sup>

For NV centers in diamond, the generation rate of coherent photons is limited by the long radiative lifetime ( $\tau_0 \simeq 12$  ns) and the small branching-ratio ( $\approx 3\%$ ) of photons into the zero-phonon line (ZPL).<sup>24</sup> Furthermore, the photon extraction efficiency out of the diamond is poor owing to total internal reflection at the diamond-air interface ( $n_d = 2.41$ ). In principle, these problems can be addressed by resonant coupling of the ZPL emission to photonic resonators with a high ratio of quality factor ( $Q$ ) to mode volume  $V$ .<sup>23,25,26</sup> The cavity enhances the ZPL emission on two grounds. First, the cavity provides a well-defined output mode, ideally a Gaussian, leading to improved detection efficiency.<sup>1,27</sup> Secondly, utilizing the Purcell effect,<sup>28</sup> a cavity resonant with the ZPL enhances the total transition rate and likewise the proportion of the photons emitted into the ZPL.<sup>23</sup>

Resonant enhancement of the ZPL has been demonstrated in photonic crystal cavities<sup>29–31</sup> and hybrid-<sup>24,32,33</sup> and microring resonators.<sup>34</sup> While these resonators offer a large Purcell factor, the NV centers suffer from poor optical coherence, compromising the

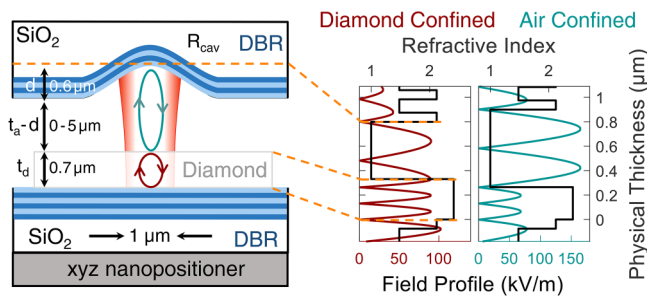


**FIG. 1.** Schematic of the diamond membrane embedded into an open Fabry-Pérot cavity. In the diamond-confined regime, the vacuum electric field is strongly confined to the diamond. Furthermore, the field profile possesses an anti-node across the diamond-air interface. In the air-confined regime, there is a field node across the diamond-air interface, and the vacuum electric field is strongly confined to the air-gap.

photon indistinguishability. This inhomogeneous broadening of the ZPL is a consequence of a fluctuating charge environment presumably caused by fabrication-induced surface damage.<sup>35–37</sup>

Open Fabry-Pérot microcavities offer an alternative to photonic crystal cavities. The required fabrication is relatively modest: only micron-sized single-crystalline membranes of the host material are required. A reasonably small mode volume and a high  $Q$ -factor can be achieved. Furthermore, the Fabry-Pérot cavity offers full *in situ* spatial and spectral tunability along with a Gaussian output mode.<sup>23,27,38</sup> As a consequence, open Fabry-Pérot cavities offer an attractive platform to enhance the emission from various single-photon emitters embedded in solid-state hosts.<sup>23,26,39–47,105</sup>

In this work, we present a diamond membrane embedded in a Fabry-Pérot microcavity operating in the so-called diamond-confined regime.<sup>43,48</sup> In this regime, there is a vacuum field anti-node at the diamond-air interface—the design is prone to scattering losses at this interface (Fig. 1). Despite this loss channel,  $Q$ -factors of more than  $10^5$  were observed for short cavity lengths at which the mode volume is  $\approx 3.9 \lambda_0^3$  ( $\lambda_0$  is the NV ZPL free-space wavelength). The high  $Q$ -factors render the cavity very sensitive to small losses, allowing the different loss mechanisms to be quantified. The measured  $Q$ -factor along with the low scattering-cross-section at the diamond surface leads us to predict a Purcell factor greater than 150 for the NV ZPL.

Although the motivation behind this work is to enhance the flux of coherent photons from NV centers in diamond, the theoretical Purcell factor depends solely on the cavity parameters. Therefore, similar results would be expected for other defect centers in crystalline hosts provided the surface losses are reduced sufficiently.

## II. METHODS

At the core of this experiment is the open microcavity, depicted schematically in Fig. 1. The device used in this experiment is conceptually the same as the device used in Refs. 23 and 27 but uses a different combination of top and bottom mirror and a different diamond membrane. The cavity mirrors were created from two

planar SiO<sub>2</sub> substrates, where for the top mirror, a CO<sub>2</sub>-laser ablation technique was used to create a matrix of atomically smooth microindentations with radius of curvature  $R_{\text{cav}} \sim 10, \dots, 30 \mu\text{m}$  (Appendix A).<sup>49,50</sup> The mirror substrates were subsequently coated with a high-reflectivity distributed Bragg reflector (DBR) coating (ECI Evapcoat) to support a target finesse  $\mathcal{F} \sim 10^4$  at the NV ZPL wavelength. The reflective stopbands were characterized using a white-light transmission measurement (Appendix A).<sup>27</sup> Using a one-dimensional transfer-matrix calculation (Essential Macleod), we are able to reconstruct the reflective stopband using  $\lambda_{\text{c,top}} = 629 \text{ nm}$  and  $\lambda_{\text{c,bot}} = 625 \text{ nm}$  as the center wavelength for the top- and bottom mirror, respectively.

The small  $R_{\text{cav}}$  supports Gaussian fundamental modes with beam waist  $\sim 1 \mu\text{m}$ , facilitating efficient mode matching to external detection optics.<sup>27,46</sup> The bottom mirror is mounted on a stack of three-axis piezoelectric nanopositioners (attocube ANPx51, ANPz51), allowing for full *in situ* spatial and spectral tunability of the standing wave inside the cavity.

Using a micromanipulator needle, we transfer a single-crystal diamond micromembrane with dimensions  $\sim 35 \times 35 \times 0.7 \mu\text{m}^3$  to the bottom mirror, where the small surface area of the diamond micromembrane facilitates strong bonding via van der Waals interactions.<sup>23</sup> We investigate the surface quality of the top-surface of the diamond membrane using atomic force microscopy (AFM). Analyzing the AFM image revealed a large-scale surface texture (period  $\sim \mu\text{m}$ ) with root-mean-square (RMS) waviness<sup>51</sup> of vertical height  $W_q = 1.6 \text{ nm}$ , which we attribute to polishing marks, and a small-scale RMS surface-roughness of  $\sigma_q = 0.3 \text{ nm}$  (period  $\sim \text{nm}$ ) (Appendix A).

To probe the cavity mode-structure, we pump the cavity using a green continuous-wave laser, whose frequency lies on the blue-side of the reflective stopband. We characterize and model the mode structure of the cavity by measuring broadband background photoluminescence (PL) from the diamond coupling to the cavity modes while stepwise reducing the width of the air-gap  $t_a$  [the inset in Fig. 2(a)].<sup>23</sup> Using one-dimensional transfer-matrix simulations (Essential Macleod), we simulate the cavity mode-structure for different diamond thicknesses  $t_d$ . We find an excellent overlap with the experimental mode-structure using  $t_d = 733 \text{ nm}$  [Fig. 2(a)]. In this experiment, the width of the air-gap was reduced until the two mirrors were in contact. By considering the depth of the crater ( $d \approx 0.64 \mu\text{m}$ , Appendix A), we extract a minimal mode number  $q_{\text{air}} = 3$  for the mode just out of contact. Here,  $q_{\text{air}}$  is the mode index in air, starting at  $q_{\text{air}} = 1$  for the first resonance, corresponding to  $t_a = 129 \text{ nm}$  for  $\lambda = 637.7 \text{ nm}$ .

The observed non-linear mode dispersion arises as a consequence of hybridization between cavity modes confined to the air-gap and diamond, respectively.<sup>48</sup> The position of the resultant avoided crossings depends on the exact diamond thickness  $t_d$ , giving rise to the “air-confined” and “diamond-confined” regimes (see Appendix B). The middle and rightmost panel in Fig. 2(a) show simulations for a diamond-confined ( $t_d = 2.75 \times \lambda_0/n_d = 727.4 \text{ nm}$ ) and for an air-confined ( $t_d = 3.00 \times \lambda_0/n_d = 793.5 \text{ nm}$ ) geometry, respectively. Here,  $\lambda_0 = 637.7 \text{ nm}$  corresponds to the NV ZPL free-space wavelength, and  $n_d = 2.41$  is the refractive index of diamond. By comparing the experimental and simulated mode-structures, it is clear that at the NV ZPL wavelength, the cavity operates in a

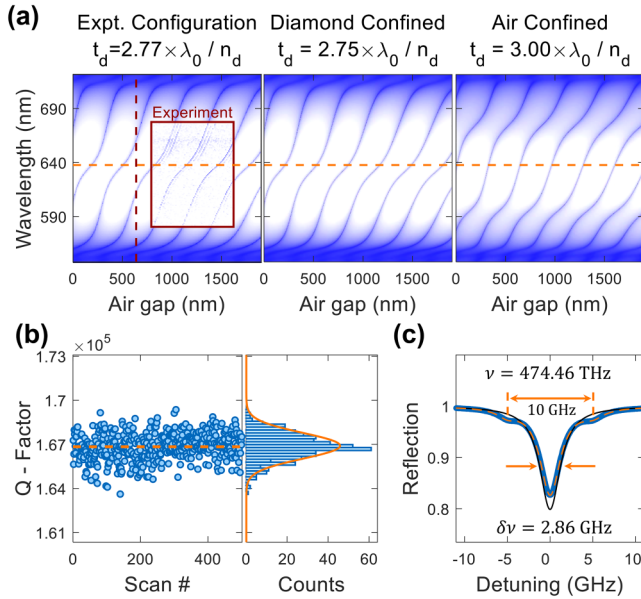


**FIG. 2.** (a) The inset in the leftmost panel shows PL as a function of cavity length under cw green excitation ( $\lambda = 532$  nm,  $P = 30$  mW). The non-linearity of the mode dispersion depends on the exact diamond thickness. The experimental mode-structure (background) is well reproduced using a one-dimensional transfer-matrix simulation with  $t_d = 733$  nm, corresponding to  $t_d = 2.77 \times \lambda_0 / n_d$  with  $\lambda_0 = 637.7$  nm. The vertical red dashed line indicates the depth of the crater ( $d = 0.64 \mu\text{m}$ ). The horizontal orange line indicates  $\lambda_0 = 637.7$  nm. The middle and rightmost panels show similar simulations for a diamond-confined ( $t_d = 2.75 \times \lambda_0 / n_d = 727$  nm) and an air-confined ( $t_d = 3.00 \times \lambda_0 / n_d = 794$  nm) cavity, respectively. By comparison to the simulations, the geometry used in this experiment is clearly diamond-confined at the NV ZPL wavelength (orange dashed line, for details, see the main text). (b) Spread of 500 individual  $Q$ -factor measurements on the diamond for mode  $q_{\text{air}} = 8$ . The data follow a Gaussian distribution centered at  $Q = 166\,900$  with a standard deviation  $\sigma = 870$ . (c) Reflection of the cavity as a function of cavity detuning for  $\lambda = 631.9$  nm. Note that the detection optics is not adjusted for perfect mode matching between the cavity mode and the incoming beam. The blue data-points are the average of all the 500 scans displayed in panel (b). The orange line shows a triple Lorentzian-fit, where the side-peaks at  $\nu_{\text{laser}} \pm 5$  GHz result from frequency modulation, which is employed as a frequency ruler. The black line is the reflected signal without any frequency modulation.

diamond-confined regime. In this configuration, the vacuum field is more strongly confined to the diamond, leading to larger coupling strengths to single-emitters. However, an inevitable consequence of this geometry is the presence of a vacuum electric-field anti-node across the diamond-air interface (Fig. 1), thereby rendering the cavity sensitive to scattering and absorption at the diamond surface.

The finesse  $\mathcal{F}$ —the round-trip performance of the cavity—is related to the  $Q$ -factor via (Appendix C)

$$Q = q_{\text{air}} \mathcal{F} + Q_0. \quad (1)$$

To determine the cavity linewidth  $\delta\nu$ , and consequently,  $Q = \nu / \delta\nu$ , we couple the output of a continuous-wave (cw) narrow-band tunable red diode laser (Toptica DL Pro 635,

$\lambda = 630\text{--}640$  nm) into the cavity. Keeping the excitation frequency  $\nu_{\text{laser}}$  fixed, we tune the cavity length across the cavity resonance while monitoring the reflected signal using a photodiode (see Appendix D). To extract the cavity linewidth, we use an electro-optic modulator (EOM, Jenoptik PM635) to create laser sidebands at  $\nu_{\text{laser}} \pm 5$  GHz, serving as a frequency ruler.<sup>52</sup> To extract reliably the cavity linewidth, the cavity is scanned across the resonance 500 times, each scan fitted independently with the sum of three Lorentzians. The  $Q$ -factor is defined as the average value of all 500 scans. Figure 2(b) shows the spread of the individually extracted  $Q$ -factors for mode number  $q_{\text{air}} = 8$  on the diamond membrane. Using a bin-size of 200 for the values of  $Q$ , the data follow a Gaussian centered around  $Q = 166\,900$  with standard deviation  $\sigma = 870$ . The blue line in Fig. 2(c) shows the average reflectivity data of all the 500 scans. Fitting a triple Lorentzian (orange line) yields an averaged cavity linewidth of  $\delta\nu_{\text{avg}} = 2.86$  GHz, which gives  $Q_{\text{avg}} = 165\,650$ , in good agreement with the average of the individual scans.

### III. RESULTS ON THE $Q$ -FACTOR

#### A. Bare cavity

In order to test our understanding of the mirrors themselves, we characterize initially the  $Q$ -factor of the bare cavity, i.e., a cavity without a diamond membrane. Figure 3(a) shows the behavior of the  $Q$ -factor as a function of increasing mode number  $q_{\text{air}}$  for fixed  $\lambda = 631.9$  nm. We observe a linear increase in  $Q$ -factor for  $q_{\text{air}} \leq 7$  as predicted by Eq. (1). We attribute the drop in  $Q$ -factor for  $q_{\text{air}} > 8$  to clipping losses at the top mirror.<sup>53</sup> Performing a linear fit for  $q_{\text{air}} \leq 7$  yields a bare-cavity finesse  $\mathcal{F}_{\text{bare}}^{\text{exp}} = 42\,500 \pm 4200$ . The simulations predict  $\mathcal{F}_{\text{bare}}^{\text{sim}} = 44\,410$ , in agreement with the experimental result to within the measurement uncertainty.

Next, we attempt to describe the dependence of the  $Q$ -factor of the bare cavity on mode number  $q_{\text{air}}$ . Upon changing the cavity length  $L_{\text{cav}}$ , the intensity beam waist at the curved mirror  $w_1$  evolves according to<sup>54</sup>

$$w_1 = \sqrt{\frac{\lambda R_{\text{cav}}}{\pi}} \times \left( \frac{R_{\text{cav}}}{L_{\text{cav}}} - 1 \right)^{-\frac{1}{4}}. \quad (2)$$

Clipping losses occur when this beam waist becomes larger than the spherical extent of the curved top mirror.<sup>53,55,56</sup> In principle, a small tilt angle  $\theta$  between the two mirrors will exacerbate clipping.<sup>57</sup> From a Gaussian optics approach,<sup>58</sup> we derive a model to estimate the clipping losses<sup>59</sup>

$$\tilde{\mathcal{L}}_{\text{clip}} = e^{-\frac{D^2}{2w_1^2}} \times \left[ 1 + \left( \frac{aD}{w_1^2} \right)^2 \right], \quad (3)$$

where  $a = R_{\text{cav}} \times \theta$  and  $D$  is the diameter of the spherical extent of the mirror. In this model, the first term accounts for clipping,<sup>53,55,58</sup> while the second term is a correction factor accounting for the tilt by angle  $\theta$ . In this model, the tilt results in a small lateral displacement of the cavity mode, thereby increasing the clipping loss. Using the exact mirror design obtained from Appendix A, we simulate the behavior of the cavity using a lossless 1D transfer-matrix simulation



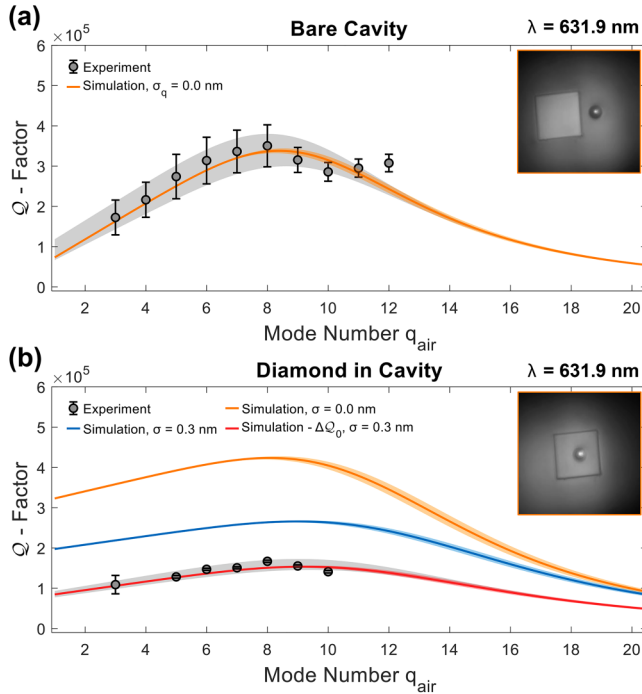


**FIG. 3.** (a) In black, the behavior of the  $Q$ -factor with increasing mode number  $q_{\text{air}}$  for the bare cavity. The  $Q$ -factor increases linearly for  $q_{\text{air}} \leq 8$ , after which clipping starts to occur. The orange line is the calculated  $Q$ -factor using a 1D transfer-matrix model. (b) Introducing the diamond into the cavity reduces the  $Q$ -factor (black data-points). Calculating the theoretical  $Q$ -factor using a lossless model (orange) and scattering with surface roughness  $\sigma_q = 0.3$  nm (blue) fail to reproduce the experimental values. The red line represents  $Q^{\text{sim}} - \Delta Q_0$  with  $\Delta Q_0 = 114\,000$  and describes the experiment well. For both panels, the black shaded regions account for the uncertainty in the fit parameters, while for the simulations, the shaded regions account for the uncertainty in the extracted tilt angle. For details, see the main text.

(Essential Macleod). The clipping losses are incorporated into the model according to  $Q_{\text{sim}} = 4\pi L_{\text{cav}} / \lambda \times (\mathcal{L}_{\text{sim}} + \mathcal{L}_{\text{clip}})^{-1}$ . To quantify the clipping losses, we perform a minimum mean-square error (MMSE) analysis and find an excellent agreement using  $D = 5.9\,\mu\text{m}$  and  $\theta_{\text{bare}} = 0-0.27^\circ$ . Including a 95% confidence interval yields a maximum tilt angle of  $0.33^\circ$ . The value of  $D$  is in good accordance with the scanning confocal-image of the mirror profile (Appendix A). The agreement between the experiment and simulation indicates that intrinsic losses in the mirrors are negligibly small compared to losses introduced by the diamond, as discussed below.

## B. Diamond membrane in the cavity

Having established the intrinsic losses in the mirrors themselves, we introduce next the diamond membrane into the cavity by moving the bottom DBR in a lateral direction. Compared to the bare cavity, we observe a reduction in both  $Q$ -factor and finesse (smaller  $\Delta Q / \Delta q_{\text{air}}$ ) with respect to the simulation [Fig. 3(b)]. Conceptually,

the diamond effectively reduces the reflectivity of the bottom DBR, thus leading to a drop in the finesse (Appendix C). Performing a linear fit for  $q_{\text{air}} \leq 7$  yields  $\mathcal{F}_{\text{diamond}}^{\text{exp}} = 11\,500 \pm 1100$ . As before, we observe clipping for  $q_{\text{air}} > 8$ . To quantify the clipping loss, we replace  $L_{\text{cav}}$  in Eq. (2) by  $L_{\text{cav}}^{\text{d}} = t_a + t_d / n_d$ <sup>55</sup> and apply Eq. (3) with  $D = 5.9\,\mu\text{m}$ . From a MMSE analysis, we calculate  $\theta_d = (0.37^{+0.15}_{-0.26})^\circ$ , where the high- and low limits are calculated from the 95% confidence interval. The larger tilt angle might suggest a small thickness-gradient in the diamond membrane.<sup>60</sup>

Contrary to the bare-cavity case, a simulation using a lossless model [orange curve in Fig. 3(b)] fails to reproduce the experimental  $Q$ -factors: the diamond membrane introduces additional loss mechanisms. Both the simulated  $Q$ -factor and the finesse ( $\mathcal{F}_{\text{perfect}}^{\text{sim}} = 17\,450$ ) are larger than observed experimentally. We, therefore, need to introduce additional losses into our model. Working in a diamond-confined regime, we expect these losses to occur at the diamond–air interface.

We investigate the role of scattering at the diamond–air interface. To this end, following the method presented in Ref. 61, we introduce a roughness of  $\sigma_q = 0.3$  nm at the diamond–air interface into the simulation (Appendix E). The choice of  $\sigma_q$  is motivated by the AFM measurement (Appendix A) and from previously reported measurements.<sup>23,27,62,63</sup> The blue line in Fig. 3(b) shows that scattering reduces both the  $Q$ -factor and the finesse ( $\mathcal{F}_{\text{scat}}^{\text{sim}} = 10\,690$ ). Interestingly, we now observe that the simulated finesse,  $\mathcal{F}_{\text{scat}}^{\text{sim}}$ , is in good accordance with the experimentally determined finesse  $\mathcal{F}^{\text{exp}}$  [equal  $\Delta Q / \Delta q_{\text{air}}$  in Fig. 3(b)], while the simulated  $Q$ -factor is larger than the experimentally determined value. We rewrite Eq. (1) as

$$Q^{\text{exp}} = Q^{\text{sim}} - \Delta Q_0. \quad (4)$$

This pragmatic approach gives an accurate representation of the experiment [red line in Fig. 3(b)] with  $\Delta Q_0 = 114\,000$ .

We now aim to understand the origin of the losses introduced by the diamond, in particular, the origin of the rigid reduction in the  $Q$ -factor described by the  $\Delta Q_0$ -term. By measuring successive cavity modes for fixed  $\lambda$  and assuming a Gaussian cavity mode, the beam waist at the bottom mirror evolves according to<sup>55</sup>

$$w_{0,\text{I}} = \sqrt{\frac{\lambda}{\pi}} \times (LR_{\text{cav}} - L^2)^{1/4}, \quad (5)$$

where  $L = t_a + t_d / n_d$ , thus probing a slightly larger surface area of the diamond.<sup>54</sup> However, the standing-wave pattern at the diamond–air interface remains unaltered. Alternatively, changing the resonant  $\lambda$  changes the standing wave inside the cavity. As scattering and absorption depend on the amplitude of the electric field, tuning the field maxima across the diamond–air interface may reveal the source of surface loss.<sup>64</sup>

To this end, we measure the dependence of the  $Q$ -factor on excitation wavelength  $\lambda$  for mode  $q_{\text{air}} = 4$  [Fig. 4(a)]. We observe a drop in the  $Q$ -factor for wavelengths away from the stopband center ( $\lambda_c = 625$  nm, Appendix A). As before, a lossless model [Fig. 4(b)] fails to reproduce the absolute value of the  $Q$ -factor as well as the dependence on  $\lambda$ .

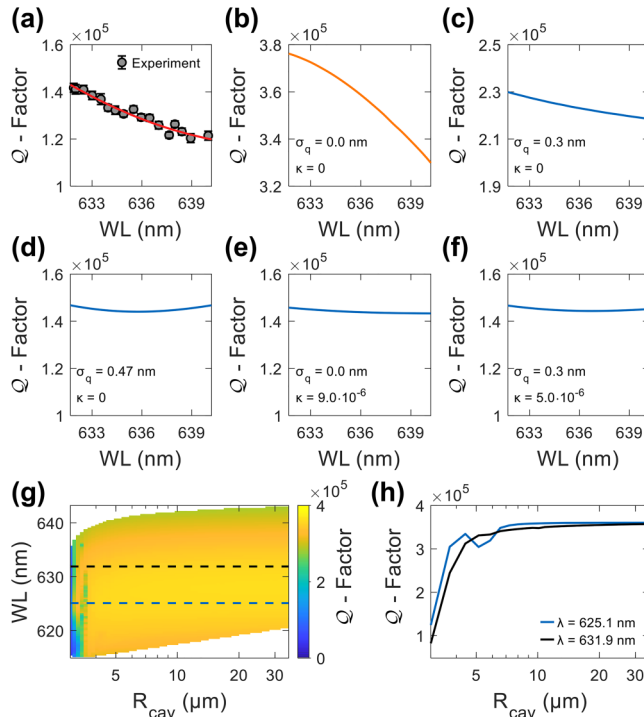


**FIG. 4.** (a) The measured  $Q$ -factor as a function of wavelength for  $q_{air} = 4$ . The  $Q$ -factor drops for excitation wavelengths away from the stopband center. The red line is a guide to the eye. (b) A calculation of the wavelength dependence of the  $Q$ -factor for a lossless cavity. (c) Introducing scattering with surface roughness  $\sigma_q = 0.3$  nm reproduces the general behavior of the experiment, but not the absolute numbers. (d)–(f) Calculations of the  $Q$ -factor with increased surface scattering ( $\sigma_q$ ) and absorption ( $\kappa$ ). (g) Calculated  $Q$ -factor as a function of wavelength and radius of curvature  $R_{cav}$  for  $q_{air} = 4$ . (h) The blue and black lines show the  $Q$ -factor at the stopband center ( $\lambda_c = 625$  nm) and for  $\lambda = 631.9$  nm, respectively. The significant drop in the  $Q$ -factor for  $R_{cav} \lesssim 5$ – $7$   $\mu$ m is attributed to clipping losses at the top mirror.

We consider enhanced diamond-related losses, surface scattering, and absorption in the diamond itself, as the origin of  $\Delta Q_0$ . In Fig. 4(d), we increase the surface roughness to  $\sigma_q = 0.47$  nm. Next, in Fig. 4(e), we include absorption in the diamond by varying the value of the extinction coefficient  $\kappa$ .<sup>61</sup> Finally, in Fig. 4(f), we combine surface scattering ( $\sigma_q = 0.3$  nm) with absorption ( $\kappa = 5.6 \times 10^{-6}$ ). All three simulations accurately account for the  $Q$ -factor at short  $\lambda$ . However, the simulations fail to reproduce the behavior with increasing  $\lambda$ . The simulations predict a minimum  $Q$ -factor for  $\lambda \sim 636$  nm beyond which an increase in the  $Q$ -factor is predicted, a feature not observed experimentally where the  $Q$ -factor monotonically decreases for longer wavelengths. It would appear, therefore, that a combination of surface roughness and absorption cannot be responsible for  $\Delta Q_0$ . Furthermore, significant absorption in the diamond is unlikely—it results in a weak dependence of the  $Q$ -factor on wavelength; yet, in the experiments, there is a strong wavelength dependence.

Another factor to consider is diffraction losses. Up until this point, only one-dimensional transfer-matrix simulations were performed: these simulations do not consider any diffraction loss at the top DBR. In addition, for tightly confined modes, the angular spread in  $k$ -space increases, leading to an increased loss in the DBR mirror and thus a reduction in the  $Q$ -factor.<sup>46</sup> To investigate this, we perform numerical simulations (COMSOL Multiphysics) of the  $Q$ -factor as a function of  $R_{cav}$  and  $\lambda$  [Fig. 4(g)]. Looking at a linecut for fixed  $\lambda$  [Fig. 4(h)], we observe a strong dependence of the  $Q$ -factor with radius for  $R_{cav} \lesssim 5$ – $7$   $\mu$ m. For larger radii, this dependence is weak, and the  $Q$ -factor saturates at  $Q = 360\,000$  in good agreement with the one-dimensional transfer-matrix simulations. We, therefore, conclude that diffraction losses at the top mirror are negligible, that the one-dimensional simulations provide reliable predictions even of the behavior of the three-dimensional cavity, and that diffraction is not responsible for  $\Delta Q_0$ .

Based on this understanding, we simulate the cavity  $Q$ -factor by including a scattering layer at the diamond–air interface with  $\sigma_q = 0.3$  nm [Fig. 4(c)], taking the absorption in the diamond and likewise any diffraction losses to be negligibly small. This approach reproduces the experimentally observed decrease of the  $Q$ -factor with  $\lambda$ .

This analysis suggests that close to the stopband center, scattering at the diamond–air interface reduces the  $Q$ -factor from an ideal value of 375 540 to 229 330. An additional loss mechanism, which results in the  $\Delta Q_0$ -term, reduces the  $Q$ -factor further to a value of 141 100. We note that if we assume that the experimental finesse matches the simulated finesse at all wavelengths, then  $\Delta Q_0$  has a small wavelength dependence, increasing monotonically by about 15% from  $\lambda = 630$  to  $\lambda = 640$  nm.

The microscopic origin of the  $\Delta Q_0$ -term is not known precisely. We speculate that it arises as a consequence of the waviness in the profile of the diamond surface (Appendix A). The spatial frequency of the waviness is comparable to that of the cavity mode—the waviness does not scatter in the same way as the surface roughness. Compatible with this hypothesis is the observation that the  $Q$ -factor is position dependent: the measured  $Q$ -factor was rather low at certain locations of the diamond membrane. In a perturbation picture,<sup>65,66</sup> the waviness mixes the fundamental mode with modes at higher frequencies. The waviness has a small spatial frequency such that it may tend to admix lossy higher lateral modes. It is an open question how the waviness might result in a rigid reduction of the  $Q$ -factor according to Eq. (4).

#### IV. PREDICTION ON THE PURCELL FACTOR

Improvements in the optical properties of an NV center in a resonant microcavity depend on the Purcell factor.<sup>28</sup> Based on the experimental results, we investigate the potential Purcell factors in a cavity of this type. To do this, we make the assumptions that better fabrication<sup>67</sup> can eliminate the losses implied in the  $\Delta Q_0$ -term; that the surface roughness of  $\sigma_q = 0.3$  nm is already excellent—some surface scattering is, therefore, inevitable; that the absorption losses in the diamond are negligible; and that we work with the mirrors from the experiment with their slight imperfections.

We need to consider the vacuum-field standing wave inside the cavity. Figure 5(a) shows the profile of the vacuum electric field

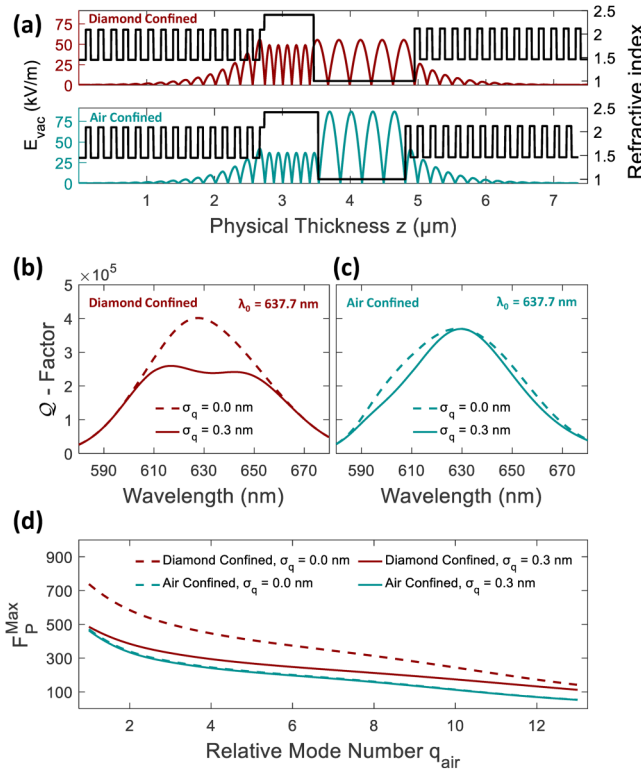


**FIG. 5.** (a) The vacuum electric-field distribution for a diamond-confined (top,  $t_d = 2.75 \times \lambda_0 / n_d = 727$  nm) and air-confined (bottom,  $t_d = 3.00 \times \lambda_0 / n_d = 794$  nm) geometry obtained from a one-dimensional transfer-matrix simulation using the mirror design extracted from Fig. 6(b). The diamond-confined case exhibits a field anti-node at the diamond-air interface, while the air-confined geometry exhibits a field node at the diamond-air interface. (b)–(c) Simulation of the  $Q$ -factor as a function of wavelength for diamond-confined (b) and air-confined (c) geometries. Introducing surface scattering with  $\sigma_q = 0.3$  nm reduces the  $Q$ -factor in the diamond-confined case, while for the air-confined geometry, the  $Q$ -factor remains relatively unaltered. (d) Expected Purcell factor as a function of mode number  $q_{\text{air}}$ .

for a diamond-confined ( $t_d = 2.75 \times \lambda_0 / n_d$ ) and air-confined ( $t_d = 3.00 \times \lambda_0 / n_d$ ) cavity, respectively. Here,  $\lambda_0 = 637.7$  nm. For the diamond-confined geometry, there is a field maximum at the diamond-air interface. Surface scattering depends on the amplitude of the electric field; thus, for  $\lambda = 637.7$  nm, scattering is maximized, resulting in a minimum  $Q$ -factor. For  $\lambda$  away from 637 nm, the field amplitude goes down; thus, the losses are reduced and the  $Q$ -factor goes up. Figures 5(b) and 5(c) show the calculated behavior of the  $Q$ -factor over a large range of  $\lambda$  for a diamond- and air-confined geometry, respectively. Introducing scattering reduces the  $Q$ -factor significantly for the diamond-confined geometry, while for the air-confined geometry, the  $Q$ -factor remains relatively unaltered.

We next estimate the expected performance of the cavity in terms of the Purcell factor  $F_P$  and the corresponding fraction of

photons emitted into the ZPL  $\eta_{\text{ZPL}}$  (see Appendix F). From Fig. 4(c), we extract  $Q = 221\,000$  for  $\lambda_0 = 637.7$  nm, which translates to  $F_P = 309$ , where the effective mode volume  $V_{\text{eff}} = 54.6(\lambda_0 / n_d)^3$  is calculated following Ref. 27 (Appendix F). Tuning the cavity into resonance with the ZPL enhances the ZPL emission rate by  $F_P$ , while the emission rate into the phonon-sideband remains unaltered. From the expected Purcell factor, we estimate  $\eta_{\text{ZPL}} = 89\%$ , compared to 2.55% in the absence of the cavity.<sup>23</sup>

The parameters of the Jaynes–Cummings Hamiltonian,  $\{g_{\text{ZPL}}, \kappa, \gamma_0\}$ , provide an alternative description of the NV-cavity coupling. Here,  $g_{\text{ZPL}}$  is the NV-cavity coupling rate,  $\kappa$  is the cavity decay rate, and  $\gamma_0$  is the spontaneous emission rate. For our system, we deduce  $\{g_{\text{ZPL}}, \kappa, \gamma_0\} = 2\pi \times \{228 \text{ MHz}, 2.13 \text{ GHz}, 12.63 \text{ MHz}\}$  (Appendix F). The condition ( $\kappa > g_{\text{ZPL}} > \gamma_0$ ) firmly places the system in the weak-coupling regime of cavity QED—a favorable condition for photon collection (Appendix G).<sup>26</sup> Finally, we calculate the expected cooperativity of our system:  $C_{\text{ZPL}} = 4g_{\text{ZPL}}^2 / (\kappa\gamma_0) = 7.7$ .<sup>68</sup>

We now compare the potential Purcell factors for diamond-confined and air-confined cavities. There is a trade-off: the diamond-confined cavity has a larger  $E_{\text{vac}}$  at the location of an optimally positioned NV center but is more sensitive to scattering at the diamond-air surface with respect to the air-confined cavity. Figure 5(d) shows a comparison between the Purcell factor for a diamond-confined and air-confined cavity ( $t_d = 2.75 \times \lambda_0$  and  $t_d = 3.00 \times \lambda_0$ , respectively). In the absence of any surface losses, the Purcell factor is significantly larger for the diamond-confined geometry compared to an air-confined geometry owing to two factors: the larger effective-length yields a higher  $Q$ -factor, and the stronger confinement of the vacuum field to the diamond yields a lower effective mode volume. However, introducing surface scattering ( $\sigma_q = 0.3$  nm as before) reduces the Purcell factor for the diamond-confined geometry, while for the air-confined geometry, the Purcell factor remains roughly the same. Despite the higher losses associated with a surface roughness of  $\sigma_q = 0.3$  nm, the calculations suggest that it is beneficial to work in a diamond-confined geometry on account of the higher Purcell factor [at, e.g.,  $q_{\text{air}} = 4$ , Fig. 5(d)]—this will result in a higher flux of coherent photons. An additional benefit of practical importance is that for the diamond-confined geometry,  $d\lambda/dt_d = 0.11$  compared to  $d\lambda/dt_a = 0.27$  for the air-confined geometry with same mode number  $q_{\text{air}}$  [Fig. 2(a)], thus rendering the cavity less susceptible to acoustic vibration.<sup>27</sup>

## V. CONCLUSIONS AND OUTLOOK

In this work, we have demonstrated the possibility of achieving high  $Q$ -factors in a low-volume Fabry–Pérot resonator in which the vacuum field is strongly confined to a diamond membrane. A  $Q$ -factor of 121 700 was achieved for  $\lambda \simeq 637$  nm for the minimum mode number,  $q_{\text{air}} = 4$  of which  $V \simeq 3.9\lambda_0^3$ . The  $Q$ -factor is lower than the  $Q$ -factor expected from the geometry alone. The main source of loss in this experiment is attributed to roughness and waviness at the diamond surface. The waviness, attributed as polishing marks, can potentially be mitigated by optimized plasma etching<sup>62,67</sup> and/or by atomic-layer deposition of a material with a refractive index less than diamond.<sup>55</sup> Deposition of

SiO<sub>2</sub> ( $n = 1.47$ ) or Al<sub>2</sub>O<sub>3</sub> ( $n = 1.77$ ) will also reduce the losses due to scattering. We note that surface passivation has previously been demonstrated to increase the  $Q$ -factor for GaAs resonators<sup>64,69,70</sup> albeit via a different mechanism.

Despite the presence of surface-related losses, the current design is capable of reaching a theoretical Purcell factor  $F_P = 170$ . If the waviness can be eliminated leaving the surface roughness the same, the current design is capable of reaching  $F_P = 309$ . Without the surface waviness but with the existing surface roughness, the Purcell factor is predicted to be higher for a diamond-confined cavity with respect to an air-confined cavity.

The motivation behind this work is to enhance the flux of coherent photons from single NV centers in diamond,<sup>23</sup> a step toward the realization of an efficient spin-photon interface.<sup>9</sup> We note that the Purcell factor presented here is universal:  $F_P$  depends solely on the cavity parameters, not on the properties of the emitter. The versatile design of the cavity allows a wide-range of solid-state single-photon emitters to be embedded,<sup>71</sup> for instance, other color centers in diamond,<sup>72–79</sup> defects in SiC,<sup>80–84</sup> rare-earth ions in a crystalline host,<sup>85–89</sup> or emitters in 2D materials.<sup>90,91</sup>

## ACKNOWLEDGMENTS

We thank Viktoria Yurgens for fruitful discussions and Lukas Sponfeldner for help with the atomic force microscopy measurements. We acknowledge financial support from the National Centre of Competence in Research (NCCR) Quantum Science and Technology (QSIT), a competence center funded by the Swiss National Science Foundation (SNF), the Swiss Nanoscience Institute (SNI), Innovative Training Network (ITN) network SpinNANO, and the European Union (EU) Quantum Flagship project ASTERIS (Grant Agreement No. 820394). D.R. acknowledges support from the SNF (Project No. P400P2\_194424). T.J. acknowledges support from the European Union's Horizon 2020 Research and Innovation Programme under Marie Skłodowska-Curie Grant Agreement No. 792853 (Hi-FrED) and support from the Polish National Agency for Academic Exchange under the Polish Returns 2019 programme (Agreement No. PPN/PPO/2019/1/00045/U/0001). A.J. acknowledges support from the European Union's Horizon 2020 Research and Innovation Programme under Marie Skłodowska-Curie Grant Agreement No. 840453 (HiFig).

## AUTHOR DECLARATIONS

### Conflict of Interest

The authors have no conflicts of interest to disclose.

## DATA AVAILABILITY

The data that support the findings of this study are available from the corresponding author upon reasonable request.

## APPENDIX A: THE OPEN MICROCAVITY

The device used in this work is an open, highly miniaturized, planar-concave microcavity (Fig. 1). To fabricate the curved top mirror, we start from a planar SiO<sub>2</sub> substrate, where a CO<sub>2</sub>-laser

ablation technique was used to create an array of atomically smooth craters with a radius of curvature  $R_{\text{cav}} \approx 10\text{--}30\ \mu\text{m}$ .<sup>49,50</sup> The profile of the crater used in this experiment was determined using a laser-scanning confocal-microscope image (Keyence Corporation, resolution  $\approx 200\ \text{nm}$ ), as displayed in Fig. 6(a). The surface profile of the radial cross section of the curved mirror can be described by

$$z(r) = -d \times \exp\left(-\frac{r^2}{2R_{\text{cav}} \times d}\right). \quad (\text{A1})$$

Fitting a truncated Gaussian [Eq. (A1)] to the surface profile yields  $R_{\text{cav}} = (19.7 \pm 2.5)\ \mu\text{m}$  and a depth  $d = 0.64\ \mu\text{m}$ . By comparison, a circular fit to the crater yields  $R_{\text{cav}} = 21.8\ \mu\text{m}$ .

After fabrication, the mirror substrates were coated with a high-reflectivity distributed Bragg reflector (DBR) coating (ECI Evapcoat), consisting of 14 (15)  $\lambda/4$  layers of SiO<sub>2</sub> ( $n_{\text{SiO}_2} = 1.46$ ) and Ta<sub>2</sub>O<sub>5</sub> ( $n_{\text{Ta}_2\text{O}_5} = 2.11$ ) for the top (bottom) mirror, respectively. The reflective coatings were characterized using the transmission from a white-light source, normalized to the transmission of an uncoated SiO<sub>2</sub> substrate [Fig. 6(b)].<sup>27</sup> Using a transfer-matrix-based calculation (Essential Macleod), we were able to reconstruct the reflective stopband based on a  $\lambda/4$  model [blue line in Fig. 6(b)]. By further allowing for a 3% tolerance on each individual layer thickness, the exact mirror structure could be reconstructed [red line in Fig. 6(b)]. From this calculation, we

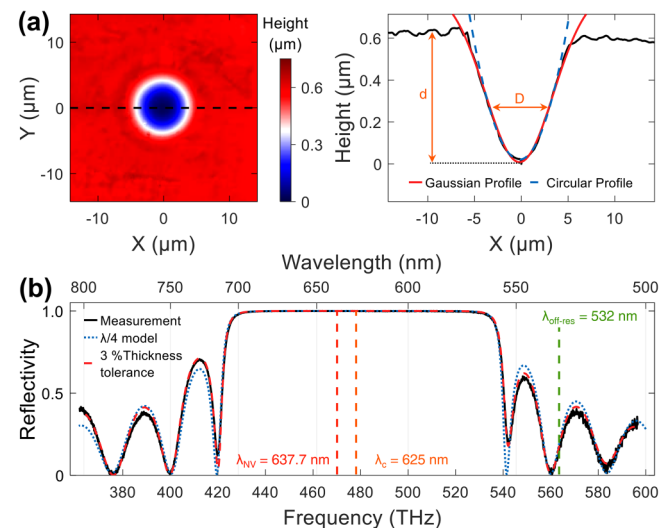


**FIG. 6.** (a) The left panel shows a laser-scanning confocal-microscope image of the crater used in this experiment. The geometrical parameters of the cavity were extracted by analyzing the surface profile along the axis of the crater (right panel). The radius  $R_{\text{cav}} = (19.7 \pm 2.5)\ \mu\text{m}$  and crater depth  $d = 0.64\ \mu\text{m}$  were extracted from a Gaussian fit [Eq. (A1), red line]. A circular fit yields  $R_{\text{cav}} = 21.8\ \mu\text{m}$  (dashed blue line). (b) Transmission measurement of the DBR mirror using a white-light source normalized to the transmission through an uncoated SiO<sub>2</sub> chip. By fitting the reflectivity spectrum using a transfer-matrix based refinement algorithm, the stopband center was determined to lie at  $\lambda_c = 625\ \text{nm}$ .



deduce a stopband center of  $\lambda_{c,bot} = 625$  nm for the bottom mirror. Following the same approach for the top mirror yields a stopband center at  $\lambda_{c,top} = 629$  nm.

Following previously reported fabrication procedures, a diamond micro-membrane with dimensions  $\sim 35 \times 35 \times 0.7 \mu\text{m}^3$  was fabricated from a  $50 \mu\text{m}$  thick commercially available single-crystalline diamond (Element six) using electron-beam lithography and inductively coupled plasma etching.<sup>62,63,92,93</sup> Post fabrication, the diamond membrane was transferred to the bottom DBR using a micro-manipulator. The Raman shift and the Raman linewidth provide evidence for a homogeneous low-strain diamond environment.<sup>27,60</sup> The small contact area, combined with a low surface roughness, facilitates bonding of the diamond membrane to the

bottom mirror via van der Waals interactions.<sup>23,27</sup> After transfer, the surface quality of the top-surface of the diamond membrane was investigated by atomic force microscopy (AFM) [Fig. 7(a)]. The surface profile [green line in Fig. 7(b)] is composed of large-scale (period  $\sim \mu\text{m}$ ) surface waviness<sup>51</sup> superimposed by small-scale surface roughness (period  $\sim \text{nm}$ ). The waviness is a consequence of the diamond polishing performed by the external manufacturer of the  $50 \mu\text{m}$  thick membranes from a  $500 \mu\text{m}$  thick substrate. To quantify further the diamond surface, we disentangle the surface waviness from the surface roughness by computing the Fourier transform of the measured surface profile. Here, we attribute surface features with spacial frequency  $\xi \leq 2 \mu\text{m}^{-1}$  (spatial wavelength  $\lambda \geq 0.5 \mu\text{m}$ ) to surface waviness and features with  $\xi > 2 \mu\text{m}^{-1}$  to surface roughness. From this analysis, we deduce surface waviness with root-mean-square (RMS) amplitude  $W_q = 1.64$  nm [pink line in Fig. 7(b)] and RMS surface roughness of  $\sigma_q = 0.32$  nm [red line in Fig. 7(b)]. We next extend this analysis to the entire AFM scan. Figure 7(c) shows the residual surface roughness after removing the low-frequency components ( $\xi \leq 2 \mu\text{m}^{-1}$ ). The green rectangle indicates a relatively large  $4.0 \times 3.5 \mu\text{m}^2$  clean area (i.e., free of dust and contaminations) with  $W_q = 1.61$  nm and  $\sigma_q = 0.31$  nm. For comparison, calculating the cavity beam waist at the diamond according to Eq. (5) yields  $w_{0,I} \simeq (1.02 - 1.22) \mu\text{m}$  for modes  $q_{\text{air}} = 4 - 10$  [Fig. 3(b)].

After characterization of the DBRs and the diamond membrane, the bottom mirror was attached to the top-surface of a three-axis piezoelectric nano-positioner (attocube), and the entire piece was then mounted inside a homebuilt titanium cage. The top mirror was glued onto a titanium holder; the holder was attached to the top of the cage with a thin layer of indium between the holder and cage. The soft indium acts as an adjustable spacer allowing the relative tilt between the two mirrors to be minimized. The piezoelectric positioners allow the microcavity length and the lateral position of the microcavity mode to be adjusted *in situ*.<sup>27,94</sup> Although all measurements in this work were carried out at room temperature, the compact design facilitates experiments in a 4 K liquid-helium bath-cryostat.<sup>23,38,39,46,70</sup>

## APPENDIX B: CAVITY MODE-STRUCTURE

To put photons into the cavity mode, we rely on the diamond as an internal light source.<sup>27</sup> We pump the diamond with a green continuous-wave laser (Laser Quantum Ventus532,  $\lambda = 532$  nm,  $P = 30$  mW) whose wavelength lies on the blue-side of the stopband of the DBRs [Fig. 6(b)]. We collect the resulting photoluminescence (PL), here background PL from the diamond, while stepwise reducing the width of the air-gap  $t_a$  by applying a positive voltage to the z-piezo. Working in a backscattering geometry, the PL signal is coupled into a single-mode fiber (Thorlabs 630HP) and then sent to a spectrometer (Princeton Instruments). A long-pass filter (Semrock LP03-532RS-25) and a dichroic mirror (Semrock, FF560-FDi01) are used to filter out the excitation laser from the PL signal.<sup>27</sup>

As a first characterization, we aim to extract the geometrical parameters of the cavity by using a simple model based on Gaussian optics.<sup>94</sup> The radius of curvature,  $R_{\text{cav}}$ , of the curved mirror can be extracted by analyzing the spacing between the fundamental ( $q, 0, 0$ ) and higher-order ( $q, n, m$ ) modes. The cavity

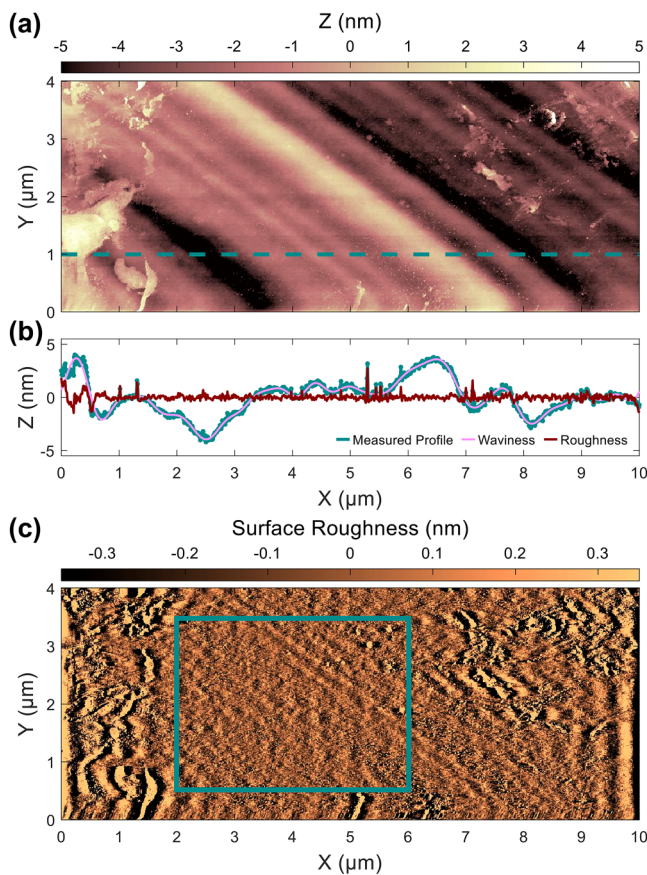


**FIG. 7.** (a) AFM measurement of the diamond membrane bonded to the bottom DBR mirror. Large-range structures attributed to polishing marks are visible. (b) The green line shows the measured surface profile along the linecut indicated by the green dashed line in (a). Computing the Fourier transform of the surface profile, and removing the high-frequency components ( $\xi < 2 \mu\text{m}^{-1}$ ), reveals surface waviness with RMS amplitude  $W_q = 1.64$  nm (pink line). The red line shows the residual short-range ( $\xi > 2 \mu\text{m}^{-1}$ ) surface roughness with an RMS amplitude of  $\sigma_q = 0.32$  nm. (c) Residual surface roughness of the image in (a) computed by removing the low-frequency components ( $\xi < 2 \mu\text{m}^{-1}$ ). The green rectangle indicates a clean area ( $4.0 \times 3.5 \mu\text{m}^2$ ) with  $W_q = 1.61$  nm and  $\sigma_q = 0.31$  nm.

length,  $L_{\text{eff}}$ , the mode number  $(q, n, m)$ , and  $R_{\text{cav}}$  are linked via<sup>27,94</sup>

$$L_{\text{eff}}(q, n, m) = \left[ q + \frac{n+m+1}{\pi} \cos^{-1}(\sqrt{g}) \right] \times \frac{\lambda_0}{2}, \quad (\text{B1})$$

where  $g = 1 - L_{\text{eff}}(q, n, m)/R_{\text{cav}}$ . Here, the effective cavity length  $L_{\text{eff}}$  is defined as the physical separation between the two mirrors, the air-gap, plus the field penetration depth into each mirror upon reflection.<sup>27,95</sup>

The mode structure exhibits two interesting features: a non-linear dispersion [an obvious feature in Fig. 2(a)] and the presence of higher-order transverse modes [weak feature in Fig. 2(a)]. By analyzing the spacing of the cavity modes [the inset of Fig. 2(a)] according to Eq. (B1), we extract a radius of curvature  $R_{\text{cav}} = 21 \mu\text{m}$ , in good agreement with the scanning confocal-microscope image shown in Fig. 6(a). We note that the detection optics were deliberately misaligned to facilitate detection of the higher-order modes [Fig. 2(a)].

The non-linear mode dispersion can be understood conceptually with a model consisting of two coupled cavities: one cavity mode is confined to the diamond by the bottom DBR and the diamond-air interface; the other cavity mode is confined to the air-gap by the diamond-air interface and the top DBR. Across the diamond-air interface, these two cavity modes couple and hybridize, resulting in the avoided crossings depicted in the inset of Fig. 2(a).<sup>48</sup>

In this coupled diamond-air cavity model, the mode structure with changing air-gap  $t_a$  and the position of the avoided crossings depend on the exact diamond thickness  $t_d$ .<sup>23,27,48</sup> For a cavity of length  $L = t_a + t_d$  (Fig. 1), fundamental resonances occur provided  $t_d n_d + t_a = j \times \lambda_0/2$ ,  $j \in \mathbb{N}$ . Depending on  $t_{a,d}$ , two regimes emerge: the so-called diamond-confined and air-confined regimes.<sup>48</sup> For the diamond-confined modes,  $t_d = (2i-1) \times \lambda_0/4$ ,  $i \in \mathbb{N}$ ; for the air-confined modes,  $t_d = i \times \lambda_0/2$ .<sup>96</sup> In the diamond-confined geometry, a change in  $t_a$  has a relatively small impact on the resonant wavelength, rendering the cavity robust against acoustic vibrations. A feature of the diamond-confined modes is that the vacuum electric-field amplitude is higher in the diamond than in the air-gap (Fig. 1), leading to a relatively high coupling strength to the NV centers ( $g_{\text{ZPL}} = d_{\text{NV}} E_{\text{vac}}$ ). However, an inevitable consequence of the diamond-confined modes is that the vacuum electric field possesses an anti-node at the diamond-air interface,<sup>43</sup> thus exacerbating losses associated with scattering or absorption at the diamond-air interface.<sup>27</sup> Conversely, in the air-confined geometry, a small change in  $t_a$  has a relatively large impact on the resonant wavelength, rendering the cavity sensitive to acoustic vibrations. A feature of the air-confined modes is that the vacuum electric field is higher in the air-gap than in the diamond, thus reducing the emitter-cavity coupling strength. In this case, there is a node in the vacuum electric field at the diamond-air interface such that the design is relatively insensitive to losses at the diamond-air interface.<sup>27</sup>

### APPENDIX C: FINESSE AND QUALITY FACTOR

The round-trip performance of the Fabry-Pérot cavity is characterized by the finesse  $\mathcal{F}$  defined as<sup>53</sup>

$$\mathcal{F} = \frac{2\pi}{\mathcal{L}_{\text{tot}}}, \quad (\text{C1})$$

where  $\mathcal{L}_{\text{tot}} = \mathcal{T}_{\text{top}} + \mathcal{T}_{\text{bot}} + \mathcal{L}_{\text{cav}}$  is the fractional energy loss per round-trip. Here,  $\mathcal{T}_{\text{top (bot)}}$  is the transmission of the top (bottom) mirror and  $\mathcal{L}_{\text{cav}}$  is the cavity round-trip-loss caused by additional loss mechanisms, such as scattering or absorption. A reliable measurement of the finesse typically requires precise knowledge of the cavity linewidth over several free-spectral ranges (FSRs). Such an experiment becomes impractical for high  $\mathcal{F}$ -values—it requires a high dynamic-range. Conversely, a measurement of the  $Q$ -factor,  $Q = \nu/\delta\nu$ , requires knowledge of the linewidth  $\delta\nu$  for one cavity-mode only, a simpler experiment. For a cavity with perfect mirrors, the  $Q$ -factor is linked to the finesse via

$$Q = \frac{2L_{\text{cav}}}{\lambda} \times \mathcal{F}. \quad (\text{C2})$$

In the experiment, we tune the thickness of the air-gap  $t_a$ ;  $t_d$  remains constant. For fixed  $\lambda$ , provided the field penetrations into the mirrors remain constant, we write  $L_{\text{cav}} = t_a + L_0$ , where  $t_a = q_{\text{air}} \times \lambda/2$ . Here,  $t_d$  and the field penetration into the mirrors are included in  $L_0$ . Thus, Eq. (C2) reduces to<sup>97</sup>

$$Q = q_{\text{air}} \times \mathcal{F} + Q_0. \quad (\text{C3})$$

In other words, a measurement of the  $Q$ -factor for subsequent modes ( $q_{\text{air}}$  and  $q_{\text{air}} + 1$ ) determines the cavity finesse.

### APPENDIX D: EXTRACTING THE CAVITY LINEWIDTH

We present some details of the experiment. The linearly polarized output of a tunable red diode laser (Toptica DL Pro 635,  $\lambda = 630\text{--}640 \text{ nm}$ ,  $\delta\nu \lesssim 500 \text{ kHz}$ ,  $P = 800 \mu\text{W}$ ) was passed through a  $\lambda/2$ -plate (B. Halle) before entering the cavity. Working in a backscattering geometry, a pellicle beam-splitter (Thorlabs BP145B1) was used to separate the reflected signal from the incident laser-beam. Keeping the excitation frequency  $\nu_{\text{laser}}$  fixed, we tune the cavity length across the resonance at a typical speed of  $8.7 \mu\text{m/s}$  ( $1.56 \text{ GHz/s}$ ), while monitoring the reflected laser light using a photodiode and a fast oscilloscope (LeCroy WaveRunner 606Zi). To calibrate the displacement of the piezo, and thus extract the cavity linewidth, we use an electro-optic modulator (EOM, Jenoptik PM635) to create laser sidebands at  $\nu_{\text{laser}} \pm 5 \text{ GHz}$ .<sup>52</sup> Here, we assume a linear behavior of cavity length with piezo-voltage across the  $10 \text{ GHz}$  bandwidth (corresponding to a change in air-gap,  $\Delta t_a = 0.056 \text{ nm}$ ).

In the bare cavity, i.e., in a cavity without a diamond membrane, for slow scanning speeds ( $\lesssim 3 \text{ GHz/s}$ ), evidence of photothermal bistability<sup>53,98</sup> was observed. The origin of this effect is likely the weak absorption in the mirror coating on the order of  $100 \text{ ppb}$ .<sup>99</sup> However, as these losses are negligible compared to the losses introduced by the diamond, the bistability was not investigated further. We note that photothermal bistability was not observed once the diamond membrane was included in the cavity.

### APPENDIX E: SIMULATING SURFACE SCATTERING

Scattering at the diamond surface can be incorporated in the one-dimensional transfer-matrix simulations following the method

reported by Ref. 61. Following this approach, we simulate scattering at the diamond–air interface by adding an additional layer on top of the diamond with thickness  $d = 2\sigma_q$  and complex refractive index  $\tilde{n} = n_{\text{eff}} + i\kappa$ . Here, the effective refractive index  $n_{\text{eff}} = \sqrt{(n_a^2 + n_d^2)/2}$  and the extinction coefficient  $\kappa$  are given by<sup>61</sup>

$$\kappa = \frac{\pi(n_a - n_d)^2(n_a + n_d)}{4n_{\text{eff}}} \times \frac{d}{\lambda}, \quad (\text{E1})$$

where  $\lambda$  is the free-space wavelength and  $n_a$  and  $n_d$  are the refractive index of the air and the diamond layer, respectively.

Scattering at the backside of the diamond is treated in the same way, by replacing  $n_a$  by  $n_{\text{TasO}_2}$ . However, the high-terminated bottom mirror leads to a field node at the diamond–mirror interface (Fig. 1), thus minimizing scattering losses at the diamond–mirror interface.

## APPENDIX F: ESTIMATING THE PURCELL FACTOR

We calculate the expected Purcell factor<sup>28</sup> for our device, following the approach presented by Refs. 23 and 27. To start, we simulate the vacuum electric-field distribution for a one-dimensional cavity using the same transfer-matrix algorithm used to simulate the  $Q$ -factor (Essential Macleod). For a Gaussian cavity mode, the vacuum electric field is quantized according to<sup>27</sup>

$$\int_{\text{cav}} \epsilon_0 \epsilon_R(z) |\vec{E}_{\text{vac}}(z)|^2 dz \int_0^{2\pi} d\phi \int_0^\infty r e^{-r^2/2w_1^2} dr = 2\pi \times \frac{1}{4} w_1^2 \int_{\text{cav}} \epsilon_0 n^2(z) |\vec{E}_{\text{vac}}(z)|^2 dz = \frac{\hbar\omega}{2}. \quad (\text{F1})$$

Here, we take  $\epsilon_R = n_d^2$  and assume a constant beam waist  $w_{0,d} \simeq 1.0 \mu\text{m}$  ( $q_{\text{air}} = 4$ ) along the length of the cavity, calculated from Eq. (5). Inside the diamond, we obtain a maximum  $|\vec{E}_{\text{vac}}| = 54.73 \text{ kV m}^{-1}$ . For an emitter located at  $\vec{r} = \vec{r}_0$ , the effective mode volume is calculated according to<sup>100,101</sup>

$$V_{\text{eff}} = \frac{\int_{\text{cav}} \epsilon_0 \epsilon_R(\vec{r}) |\vec{E}_{\text{vac}}(\vec{r})|^2 d^3r}{\epsilon_0 \epsilon_R(\vec{r}_0) |\vec{E}_{\text{vac}}(\vec{r}_0)|^2} = \frac{\hbar\omega/2}{\epsilon_0 \epsilon_R(\vec{r}_0) |\vec{E}_{\text{vac}}(\vec{r}_0)|^2}. \quad (\text{F2})$$

Numerically, we obtain  $V_{\text{eff}} = 54.57 (\lambda_0/n_d)^3$ . For the experimental geometry,  $Q_{\sigma_q=0.3 \text{ nm}}^{\text{sim}} = 221\,000$  for  $\lambda = 637.7 \text{ nm}$  [ $q_{\text{air}} = 4$ , Fig. 4(c)], from which we deduce

$$F_P = 1 + \frac{3}{4\pi^2} \frac{Q_{\sigma_q=0.3 \text{ nm}}^{\text{sim}}}{V_{\text{eff}}} \left( \frac{\lambda_0}{n_d} \right)^3 = 309. \quad (\text{F3})$$

The probability of emission into the cavity mode for an emitter with 100% quantum efficiency is given by the  $\beta$ -factor:  $\beta = (F_P - 1)/F_P = 0.9968$ . We note that the Purcell factor is independent of any emitter properties: the calculation is based solely on the experimental cavity parameters.<sup>68</sup>

Next, we apply the calculated Purcell factor to an NV center: we are interested in calculating the emission rate into the ZPL. We assume that the NV center's optical dipole is aligned along the polarization-axis of the cavity mode. In the absence of the cavity, the excited-state decay rate is  $\gamma_0$ , consisting of radiative decay into the ZPL (rate  $\xi_0\gamma_0$  where  $\xi_0$  is the Debye–Waller factor) and all other decay processes [rate  $(1 - \xi_0)\gamma_0$ ]. Tuning the cavity on resonance with the ZPL enhances the ZPL emission by  $F_P$ , while the emission into the phonon-sideband remains unaltered. Therefore, in the presence of the cavity, the decay rate becomes  $\gamma_{\text{cav}} = F_P \xi_0 \gamma_0 + (1 - \xi_0)\gamma_0$ , where  $F_P$  is defined according to Eq. (F3).<sup>26</sup> Taking the ratio of the decay rate in the cavity to that of free space yields

$$\frac{\gamma_{\text{cav}}}{\gamma_0} = \frac{\tau_0}{\tau_{\text{cav}}} = 1 + \xi_0(F_P - 1), \quad (\text{F4})$$

where  $\tau_{\text{cav}}$  is the radiative lifetime in the cavity. Taking the unperturbed lifetime  $\tau_0 = 12.6 \text{ ns}$  and  $\xi_0 = 2.55\%$ <sup>23</sup> along with  $F_P = 309$ , Eq. (F4) predicts an reduction in lifetime to  $\tau_{\text{cav}} = 1.42 \text{ ns}$ . The reduction in lifetime results in broadening of the homogeneous linewidth from  $\Delta\nu_0^{\text{ZPL}} = \gamma_0/(2\pi) = 12.6 \text{ MHz}$  to  $\Delta\nu_{\text{cav}}^{\text{ZPL}} = [1 + \xi_0(F_P - 1)] \times \gamma_0/(2\pi) = 112 \text{ MHz}$ , rendering the NV less sensitive to spectral wandering. We next calculate the efficiency,  $\eta_{\text{ZPL}}$ , of emitting a photon into the ZPL;<sup>26</sup>  $\eta_{\text{ZPL}} = F_P \times \xi_0 \gamma_0 / \gamma_{\text{cav}} = \xi_0 F_P / (\xi_0(F_P - 1) + 1) = 89.0\%$ . Finally, we estimate the cooperativity of the ZPL,  $C_{\text{ZPL}}$ , for our system. Using the definition  $F_P = 1 + C_{\text{ZPL}}/\xi_0$ <sup>26</sup> yields  $C_{\text{ZPL}} = 7.8$ . This cooperativity is larger than those achieved so far using an open microcavity. Neglecting inhomogeneous broadening,  $C_{\text{ZPL}} = 0.90$  (Riedel *et al.*<sup>23</sup>) and  $C_{\text{ZPL}} = 0.08$  (Ruf *et al.*<sup>26</sup>). We note that in practice, inhomogeneous broadening (rate  $\gamma^*$ ) reduces the value in the experiment ( $\gamma_0 \rightarrow \gamma_0 + \gamma^*$ <sup>102,103</sup>) to  $C_{\text{ZPL}} = 0.011$  ( $\gamma^* = 2\pi \times 1 \text{ GHz}$ <sup>23</sup>) and  $C_{\text{ZPL}} = 0.0067$  ( $\gamma^* = 2\pi \times 190 \text{ MHz}$ <sup>26</sup>), respectively.

Alternatively, the NV-cavity coupling can be described with the Jaynes–Cummings Hamiltonian in terms of  $\{g_{\text{ZPL}}, \kappa, \gamma_0\}$ : where  $g_{\text{ZPL}} = d_{\text{NV}} E_{\text{vac}}$  is the NV-cavity coupling rate,  $\kappa$  is the cavity decay rate, and  $\gamma_0$  is, as before, the spontaneous emission rate.<sup>6,104</sup> Using  $d_{\text{NV}}/e = \sqrt{\epsilon_0} 0.108 \text{ nm}$ ,<sup>23</sup> we deduce  $\{g_{\text{ZPL}}, \kappa, \gamma_0\} = 2\pi \times \{228 \text{ MHz}, 2.13 \text{ GHz}, 12.63 \text{ MHz}\}$ , firmly placing the system in the weak-coupling regime of cavity QED. The condition ( $\kappa > g_{\text{ZPL}} > \gamma_0$ ) is favorable for photon collection (Appendix G).<sup>26</sup> This approach results in  $\eta_{\text{ZPL}} = (4g_{\text{ZPL}}^2/(\kappa\gamma_0)) / (4g_{\text{ZPL}}^2/(\kappa\gamma_0) + 1) = 88.6\%$  and  $C_{\text{ZPL}} = 4g_{\text{ZPL}}^2/(\kappa\gamma_0) = 7.7$ <sup>68</sup> and gives the same numerical values as above.

## APPENDIX G: ESTIMATING THE CAVITY OUTCOUPLING EFFICIENCY

The ultimate aim is to maximize the outcoupling efficiency, i.e., the probability of creating a photon on the outside of the top mirror following NV decay into the ZPL. The cavity should be made asymmetric such that the loss rate through the top mirror is larger than the loss rate through the bottom mirror,  $\kappa_{\text{top}} \gg \kappa_{\text{bot}}$ . Given the high quality of the dielectric DBRs [see Fig. 3(a)], this is easy to achieve. Ideally,  $\kappa_{\text{top}}$  is also much larger than the unwanted scattering losses,  $\kappa_{\text{loss}}$ . For a given  $g_{\text{ZPL}}$ ,  $\gamma_0$  and  $\kappa_{\text{loss}}$ , and assuming  $\kappa_{\text{top}} \gg \kappa_{\text{loss}}$ , the outcoupling efficiency  $\eta$  can be maximized by



choosing  $\kappa_{\text{top}} = \kappa_{\text{top}}^{\text{opt}}$ , where<sup>46</sup>

$$\kappa_{\text{top}}^{\text{opt}} = \sqrt{\left(1 + \frac{\kappa_{\text{loss}}}{\gamma_0}\right) \times (4g_{\text{ZPL}}^2 + \kappa_{\text{loss}}\gamma_0)}. \quad (\text{G1})$$

For  $\{g_{\text{ZPL}}, \kappa_{\text{loss}}, \gamma_0\} = 2\pi\{228 \text{ MHz}, 777 \text{ MHz}, 12.6 \text{ MHz}\}$ , the values determined here,  $\kappa_{\text{top}}^{\text{opt}} = 2\pi \times 3.69 \text{ GHz}$ . Reassuringly,  $\kappa_{\text{top}}^{\text{opt}}$  is larger than  $\kappa_{\text{loss}}$ . This results in a high  $\eta$ . With  $\kappa_{\text{top}} = \kappa_{\text{top}}^{\text{opt}}$ , we find  $\kappa_{\text{tot}}^{\text{opt}} = 2\pi \times 5.49 \text{ GHz}$  ( $\mathcal{Q}_{\text{opt}} = 85\,650$ ),  $F_p = 120$  [Eq. (F3)],  $C_{\text{ZPL}} = 3.04$ , and

$$\eta = \frac{4g_{\text{ZPL}}^2/(\kappa_{\text{tot}}^{\text{opt}}\gamma_0)}{4g_{\text{ZPL}}^2/(\kappa_{\text{tot}}^{\text{opt}}\gamma_0) + 1} \times \frac{\kappa_{\text{top}}^{\text{opt}}}{\kappa_{\text{tot}}^{\text{opt}} + \gamma_0} = 50.9\%. \quad (\text{G2})$$

## REFERENCES

- <sup>1</sup>W. B. Gao, A. Imamoglu, H. Bernien, and R. Hanson, "Coherent manipulation, measurement and entanglement of individual solid-state spins using optical fields," *Nat. Photonics* **9**, 363–373 (2015).
- <sup>2</sup>M. Atatüre, D. Englund, N. Vamivakas, S.-Y. Lee, and J. Wrachtrup, "Material platforms for spin-based photonic quantum technologies," *Nat. Rev. Mater.* **3**, 38–51 (2018).
- <sup>3</sup>C. Simon, "Towards a global quantum network," *Nat. Photonics* **11**, 678–680 (2017).
- <sup>4</sup>H. J. Kimble, "The quantum internet," *Nature* **453**, 1023–1030 (2008).
- <sup>5</sup>S. Wehner, D. Elkouss, and R. Hanson, "Quantum internet: A vision for the road ahead," *Science* **362**, eaam9288 (2018).
- <sup>6</sup>A. Reiserer and G. Rempe, "Cavity-based quantum networks with single atoms and optical photons," *Rev. Mod. Phys.* **87**, 1379–1418 (2015).
- <sup>7</sup>W. J. Munro, K. Azuma, K. Tamaki, and K. Nemoto, "Inside quantum repeaters," *IEEE J. Sel. Top. Quantum Electron.* **21**, 78–90 (2015).
- <sup>8</sup>M. K. Bhaskar, R. Riedinger, B. Machielse, D. S. Levonian, C. T. Nguyen, E. N. Knall, H. Park, D. Englund, M. Lončar, D. D. Sukachev, and M. D. Lukin, "Experimental demonstration of memory-enhanced quantum communication," *Nature* **580**, 60–64 (2020).
- <sup>9</sup>D. D. Awschalom, R. Hanson, J. Wrachtrup, and B. B. Zhou, "Quantum technologies with optically interfaced solid-state spins," *Nat. Photonics* **12**, 516–527 (2018).
- <sup>10</sup>G. Balasubramanian, P. Neumann, D. Twitchen, M. Markham, R. Kolesov, N. Mizuochi, J. Isoya, J. Achard, J. Beck, J. Tisler, V. Jacques, P. R. Hemmer, F. Jelezko, and J. Wrachtrup, "Ultralong spin coherence time in isotopically engineered diamond," *Nat. Mater.* **8**, 383–387 (2009).
- <sup>11</sup>N. Bar-Gill, L. Pham, A. Jarmola, D. Budker, and R. Walsworth, "Solid-state electronic spin coherence time approaching one second," *Nat. Commun.* **4**, 1743 (2013).
- <sup>12</sup>L. Robledo, L. Childress, H. Bernien, B. Hensen, P. F. A. Alkemade, and R. Hanson, "High-fidelity projective read-out of a solid-state spin quantum register," *Nature* **477**, 574–578 (2011).
- <sup>13</sup>Y. Chu, M. Markham, D. J. Twitchen, and M. D. Lukin, "All-optical control of a single electron spin in diamond," *Phys. Rev. A* **91**, 021801 (2015).
- <sup>14</sup>D. M. Irber, F. Poggiali, F. Kong, M. Kieschnick, T. Lühmann, D. Kwiatkowski, J. Meijer, J. Du, F. Shi, and F. Reinhard, "Robust all-optical single-shot readout of nitrogen-vacancy centers in diamond," *Nat. Commun.* **12**, 532 (2021).
- <sup>15</sup>P. C. Maurer, G. Kucsko, C. Latta, L. Jiang, N. Y. Yao, S. D. Bennett, F. Pastawski, D. Hunger, N. Chisholm, M. Markham, D. J. Twitchen, J. I. Cirac, and M. D. Lukin, "Room-temperature quantum bit memory exceeding one second," *Science* **336**, 1283–1286 (2012).
- <sup>16</sup>T. H. Taminiau, J. Cramer, T. van der Sar, V. V. Dobrovitski, and R. Hanson, "Universal control and error correction in multi-qubit spin registers in diamond," *Nat. Nanotechnol.* **9**, 171–176 (2014).
- <sup>17</sup>S. Yang, Y. Wang, D. D. B. Rao, T. Hien Tran, A. S. Momenzadeh, M. Markham, D. J. Twitchen, P. Wang, W. Yang, R. Stöhr, P. Neumann, H. Kosaka, and J. Wrachtrup, "High-fidelity transfer and storage of photon states in a single nuclear spin," *Nat. Photonics* **10**, 507–511 (2016).
- <sup>18</sup>M. H. Abobeih, J. Cramer, M. A. Bakker, N. Kalb, M. Markham, D. J. Twitchen, and T. H. Taminiau, "One-second coherence for a single electron spin coupled to a multi-qubit nuclear-spin environment," *Nat. Commun.* **9**, 2552 (2018).
- <sup>19</sup>C. E. Bradley, J. Randall, M. H. Abobeih, R. C. Berrevoets, M. J. Degen, M. A. Bakker, M. Markham, D. J. Twitchen, and T. H. Taminiau, "A ten-qubit solid-state spin register with quantum memory up to one minute," *Phys. Rev. X* **9**, 031045 (2019).
- <sup>20</sup>L. Childress, J. M. Taylor, A. S. Sørensen, and M. D. Lukin, "Fault-tolerant quantum repeaters with minimal physical resources and implementations based on single-photon emitters," *Phys. Rev. A* **72**, 052330 (2005).
- <sup>21</sup>L. Childress, J. M. Taylor, A. S. Sørensen, and M. D. Lukin, "Fault-tolerant quantum communication based on solid-state photon emitters," *Phys. Rev. Lett.* **96**, 070504 (2006).
- <sup>22</sup>M. Pompili, S. L. N. Hermans, S. Baier, H. K. C. Beukers, P. C. Humphreys, R. N. Schouten, R. F. L. Vermeulen, M. J. Tiggeleman, L. dos Santos Martins, B. Dirkse, S. Wehner, and R. Hanson, "Realization of a multinode quantum network of remote solid-state qubits," *Science* **372**, 259–264 (2021).
- <sup>23</sup>D. Riedel, I. Söllner, B. J. Shields, S. Starsieles, P. Appel, E. Neu, P. Maletinsky, and R. J. Warburton, "Deterministic enhancement of coherent photon generation from a nitrogen-vacancy center in ultrapure diamond," *Phys. Rev. X* **7**, 031040 (2017).
- <sup>24</sup>P. E. Barclay, K.-M. C. Fu, C. Santori, A. Faraon, and R. G. Beausoleil, "Hybrid nanocavity resonant enhancement of color center emission in diamond," *Phys. Rev. X* **1**, 011007 (2011).
- <sup>25</sup>C.-H. Su, A. D. Greentree, and L. C. L. Hollenberg, "Towards a picosecond transform-limited nitrogen-vacancy based single photon source," *Opt. Express* **16**, 6240 (2008).
- <sup>26</sup>M. Ruf, M. Weaver, S. van Dam, and R. Hanson, "Resonant excitation and purcell enhancement of coherent nitrogen-vacancy centers coupled to a Fabry-Perot microcavity," *Phys. Rev. Appl.* **15**, 024049 (2021).
- <sup>27</sup>D. Riedel, S. Flågan, P. Maletinsky, and R. J. Warburton, "Cavity-enhanced Raman scattering for *in situ* alignment and characterization of solid-state microcavities," *Phys. Rev. Appl.* **13**, 014036 (2020).
- <sup>28</sup>E. M. Purcell, H. C. Torrey, and R. V. Pound, "Resonance absorption by nuclear magnetic moments in a solid," *Phys. Rev.* **69**, 37–38 (1946).
- <sup>29</sup>A. Faraon, C. Santori, Z. Huang, V. M. Acosta, and R. G. Beausoleil, "Coupling of nitrogen-vacancy centers to photonic crystal cavities in monocrystalline diamond," *Phys. Rev. Lett.* **109**, 033604 (2012).
- <sup>30</sup>J. Riedrich-Möller, S. Pezzagna, J. Meijer, C. Pauly, F. Mücklich, M. Markham, A. M. Edmonds, and C. Becher, "Nanoimplantation and purcell enhancement of single nitrogen-vacancy centers in photonic crystal cavities in diamond," *Appl. Phys. Lett.* **106**, 221103 (2015).
- <sup>31</sup>T. Jung, J. Görlitz, B. Kambs, C. Pauly, N. Raatz, R. Nelz, E. Neu, A. M. Edmonds, M. Markham, F. Mücklich, J. Meijer, and C. Becher, "Spin measurements of NV centers coupled to a photonic crystal cavity," *APL Photonics* **4**, 120803 (2019).
- <sup>32</sup>M. Gould, E. R. Schmidgall, S. Dadgostar, F. Hatami, and K.-M. C. Fu, "Efficient extraction of zero-phonon-line photons from single nitrogen-vacancy centers in an integrated GaP-on-diamond platform," *Phys. Rev. Appl.* **6**, 011001 (2016).
- <sup>33</sup>E. R. Schmidgall, S. Chakravarthi, M. Gould, I. R. Christen, K. Hestroffer, F. Hatami, and K.-M. C. Fu, "Frequency control of single quantum emitters in integrated photonic circuits," *Nano Lett.* **18**, 1175–1179 (2018).
- <sup>34</sup>A. Faraon, P. E. Barclay, C. Santori, K.-M. C. Fu, and R. G. Beausoleil, "Resonant enhancement of the zero-phonon emission from a colour centre in a diamond cavity," *Nat. Photonics* **5**, 301–305 (2011).
- <sup>35</sup>M. Kasperczyk, J. A. Zuber, A. Barfuss, J. Kölbl, V. Yurgens, S. Flågan, T. Jakubczyk, B. Shields, R. J. Warburton, and P. Maletinsky, "Statistically modeling optical linewidths of nitrogen vacancy centers in microstructures," *Phys. Rev. B* **102**, 075312 (2020).



- <sup>36</sup>V. Yurgens, J. A. Zuber, S. Flågan, M. De Luca, B. J. Shields, I. Zardo, P. Maletinsky, R. J. Warburton, and T. Jakubczyk, "Low-charge-noise nitrogen-vacancy centers in diamond created using laser writing with a solid-immersion lens," *ACS Photonics* **8**, 1726–1734 (2021).
- <sup>37</sup>S. Chakravarthi, C. Pederson, Z. Kazi, A. Ivanov, and K.-M. C. Fu, "Impact of surface and laser-induced noise on the spectral stability of implanted nitrogen-vacancy centers in diamond," *Phys. Rev. B* **104**, 085425 (2021).
- <sup>38</sup>R. J. Barbour, P. A. Dalgarno, A. Curran, K. M. Nowak, H. J. Baker, D. R. Hall, N. G. Stoltz, P. M. Petroff, and R. J. Warburton, "A tunable microcavity," *J. Appl. Phys.* **110**, 053107 (2011).
- <sup>39</sup>L. Greuter, S. Starosielec, A. V. Kuhlmann, and R. J. Warburton, "Towards high-cooperativity strong coupling of a quantum dot in a tunable microcavity," *Phys. Rev. B* **92**, 045302 (2015).
- <sup>40</sup>D. Wang, H. Kelkar, D. Martin-Cano, T. Utikal, S. Götzinger, and V. Sandoghdar, "Coherent coupling of a single molecule to a scanning Fabry-Perot microcavity," *Phys. Rev. X* **7**, 021014 (2017).
- <sup>41</sup>D. Wang, H. Kelkar, D. Martin-Cano, D. Rattenbacher, A. Shkarin, T. Utikal, S. Götzinger, and V. Sandoghdar, "Turning a molecule into a coherent two-level quantum system," *Nat. Phys.* **15**, 483–489 (2019).
- <sup>42</sup>B. Casabone, C. Deshmukh, S. Liu, D. Serrano, A. Ferrier, T. Hümmer, P. Goldner, D. Hunger, and H. de Riedmatten, "Dynamic control of Purcell enhanced emission of erbium ions in nanoparticles," *Nat. Commun.* **12**, 3570 (2021).
- <sup>43</sup>R. Høy Jensen, E. Janitz, Y. Fontana, Y. He, O. Gobron, I. P. Radko, M. Bhaskar, R. Evans, C. D. Rodríguez Rosenblueth, L. Childress, A. Huck, and U. Lund Andersen, "Cavity-enhanced photon emission from a single germanium-vacancy center in a diamond membrane," *Phys. Rev. Appl.* **13**, 064016 (2020).
- <sup>44</sup>B. Merkel, A. Ulanowski, and A. Reiserer, "Coherent and Purcell-enhanced emission from erbium dopants in a cryogenic high-*Q* resonator," *Phys. Rev. X* **10**, 041025 (2020).
- <sup>45</sup>A. Pscherer, M. Meierhofer, D. Wang, H. Kelkar, D. Martín-Cano, T. Utikal, S. Götzinger, and V. Sandoghdar, "Single-molecule vacuum Rabi splitting: Four-wave mixing and optical switching at the single-photon level," *Phys. Rev. Lett.* **127**, 133603 (2021).
- <sup>46</sup>N. Tömm, A. Javadi, N. O. Antoniadis, D. Najer, M. C. Löbl, A. R. Korsch, R. Schott, S. R. Valentin, A. D. Wieck, A. Ludwig, and R. J. Warburton, "A bright and fast source of coherent single photons," *Nat. Nanotechnol.* **16**, 399–403 (2021).
- <sup>47</sup>S. Häußler, G. Bayer, R. Waltrich, N. Mendelson, C. Li, D. Hunger, I. Aharonovich, and A. Kubanek, "Tunable fiber-cavity enhanced photon emission from defect centers in hBN," *Adv. Opt. Mater.* **9**, 2002218 (2021).
- <sup>48</sup>E. Janitz, M. Ruf, M. Dimock, A. Bourassa, J. Sankey, and L. Childress, "Fabry-Perot microcavity for diamond-based photonics," *Phys. Rev. A* **92**, 043844 (2015).
- <sup>49</sup>D. Hunger, C. Deutsch, R. J. Barbour, R. J. Warburton, and J. Reichel, "Laser micro-fabrication of concave, low-roughness features in silica," *AIP Adv.* **2**, 012119 (2012).
- <sup>50</sup>D. Najer, M. Renggli, D. Riedel, S. Starosielec, and R. J. Warburton, "Fabrication of mirror templates in silica with micron-sized radii of curvature," *Appl. Phys. Lett.* **110**, 011101 (2017).
- <sup>51</sup>D. J. Whitehouse, *Surfaces and Their Measurement*, 1st ed. (Butterworth-Heinemann, 2002).
- <sup>52</sup>S. Bogdanović, S. B. van Dam, C. Bonato, L. C. Coenen, A.-M. J. Zwerver, B. Hensen, M. S. Z. Liddy, T. Fink, A. Reiserer, M. Lončar, and R. Hanson, "Design and low-temperature characterization of a tunable microcavity for diamond-based quantum networks," *Appl. Phys. Lett.* **110**, 171103 (2017).
- <sup>53</sup>D. Hunger, T. Steinmetz, Y. Colombe, C. Deutsch, T. W. Hänsch, and J. Reichel, "A fiber Fabry-Perot cavity with high finesse," *New J. Phys.* **12**, 065038 (2010).
- <sup>54</sup>W. Nagourney, *Quantum Electronics for Atomic Physics and Telecommunication*, 2nd ed. (Oxford University Press, 2014).
- <sup>55</sup>S. B. van Dam, M. Ruf, and R. Hanson, "Optimal design of diamond-air microcavities for quantum networks using an analytical approach," *New J. Phys.* **20**, 115004 (2018).
- <sup>56</sup>K. Durak, C. H. Nguyen, V. Leong, S. Straupe, and C. Kurtsiefer, "Diffraction-limited Fabry-Perot cavity in the near concentric regime," *New J. Phys.* **16**, 103002 (2014).
- <sup>57</sup>L. Flatten, A. Trichet, and J. Smith, "Spectral engineering of coupled open-access microcavities," *Laser Photonics Rev.* **10**, 257–263 (2016).
- <sup>58</sup>A. E. Siegman, *Lasers* (University Science Books, Mill Valley, CA, 1986).
- <sup>59</sup>S. Flågan, "An open microcavity for diamond-based photonics," Ph.D. thesis (University of Basel, 2021).
- <sup>60</sup>S. Flågan, P. Maletinsky, R. J. Warburton, and D. Riedel, "Widely-tunable, doubly-resonant Raman scattering on diamond in an open microcavity," *arXiv:2110.06242* (2021).
- <sup>61</sup>C. K. Carniglia and D. G. Jensen, "Single-layer model for surface roughness," *Appl. Opt.* **41**, 3167 (2002).
- <sup>62</sup>P. Appel, E. Neu, M. Ganzhorn, A. Barfuss, M. Batzer, M. Gratz, A. Tschöpe, and P. Maletinsky, "Fabrication of all diamond scanning probes for nanoscale magnetometry," *Rev. Sci. Instrum.* **87**, 063703 (2016).
- <sup>63</sup>D. Riedel, D. Rohner, M. Ganzhorn, T. Kaldewey, P. Appel, E. Neu, R. J. Warburton, and P. Maletinsky, "Low-loss broadband antenna for efficient photon collection from a coherent spin in diamond," *Phys. Rev. Appl.* **2**, 064011 (2014).
- <sup>64</sup>D. Najer, N. Tömm, A. Javadi, A. R. Korsch, B. Petrak, D. Riedel, V. Dolique, S. R. Valentin, R. Schott, A. D. Wieck, A. Ludwig, and R. J. Warburton, "Suppression of surface-related loss in a gated semiconductor microcavity," *Phys. Rev. Appl.* **15**, 044004 (2021).
- <sup>65</sup>D. Kleckner, W. T. M. Irvine, S. S. R. Oemrawsingh, and D. Bouwmeester, "Diffraction-limited high-finesse optical cavities," *Phys. Rev. A* **81**, 043814 (2010).
- <sup>66</sup>J. Benedikter, T. Hümmer, M. Mader, B. Schleder, J. Reichel, T. W. Hänsch, and D. Hunger, "Transverse-mode coupling and diffraction loss in tunable Fabry-Perot microcavities," *New J. Phys.* **17**, 053051 (2015).
- <sup>67</sup>S. Sangtawesin, B. L. Dwyer, S. Srinivasan, J. J. Allred, L. V. Rodgers, K. De Greve, A. Stacey, N. Dontschuk, K. M. O'Donnell, D. Hu, D. A. Evans, C. Jaye, D. A. Fischer, M. L. Markham, D. J. Twitchen, H. Park, M. D. Lukin, and N. P. de Leon, "Origins of diamond surface noise probed by correlating single-spin measurements with surface spectroscopy," *Phys. Rev. X* **9**, 031052 (2019).
- <sup>68</sup>E. Janitz, M. K. Bhaskar, and L. Childress, "Cavity quantum electrodynamics with color centers in diamond," *Optica* **7**, 1232 (2020).
- <sup>69</sup>B. Guha, F. Marsault, F. Cadiz, L. Morgenroth, V. Ulin, V. Berkovitz, A. Lemaître, C. Gomez, A. Amo, S. Combrié, B. Gérard, G. Leo, and I. Favero, "Surface-enhanced gallium arsenide photonic resonator with quality factor of  $6 \times 10^5$ ," *Optica* **4**, 218 (2017).
- <sup>70</sup>D. Najer, I. Söllner, P. Sekatski, V. Dolique, M. C. Löbl, D. Riedel, R. Schott, S. Starosielec, S. R. Valentin, A. D. Wieck, N. Sangouard, A. Ludwig, and R. J. Warburton, "A gated quantum dot strongly coupled to an optical microcavity," *Nature* **575**, 622–627 (2019).
- <sup>71</sup>I. Aharonovich, D. Englund, and M. Toth, "Solid-state single-photon emitters," *Nat. Photonics* **10**, 631–641 (2016).
- <sup>72</sup>I. Aharonovich, S. Castelletto, D. A. Simpson, C.-H. Su, A. D. Greentree, and S. Praver, "Diamond-based single-photon emitters," *Rep. Prog. Phys.* **74**, 076501 (2011).
- <sup>73</sup>T. Iwasaki, Y. Miyamoto, T. Taniguchi, P. Siyushev, M. H. Metsch, F. Jelezko, and M. Hatano, "Tin-vacancy quantum emitters in diamond," *Phys. Rev. Lett.* **119**, 253601 (2017).
- <sup>74</sup>B. C. Rose, D. Huang, Z.-H. Zhang, P. Stevenson, A. M. Tyryshkin, S. Sangtawesin, S. Srinivasan, L. Loudin, M. L. Markham, A. M. Edmonds, D. J. Twitchen, S. A. Lyon, and N. P. de Leon, "Observation of an environmentally insensitive solid-state spin defect in diamond," *Science* **361**, 60–63 (2018).
- <sup>75</sup>C. Bradac, W. Gao, J. Forneris, M. E. Trusheim, and I. Aharonovich, "Quantum nanophotonics with group IV defects in diamond," *Nat. Commun.* **10**, 5625 (2019).
- <sup>76</sup>M. E. Trusheim, N. H. Wan, K. C. Chen, C. J. Ciccarino, J. Flick, R. Sundararaman, G. Malladi, E. Bersin, M. Walsh, B. Lienhard, H. Bakhr, P. Narang, and D. Englund, "Lead-related quantum emitters in diamond," *Phys. Rev. B* **99**, 075430 (2019).

- <sup>77</sup>S. Baier, C. E. Bradley, T. Middelburg, V. V. Dobrovitski, T. H. Taminiau, and R. Hanson, "Orbital and spin dynamics of single neutrally-charged nitrogen-vacancy centers in diamond," *Phys. Rev. Lett.* **125**, 193601 (2020).
- <sup>78</sup>D. Chen, N. Zheludev, and W. Gao, "Building blocks for quantum network based on group-IV split-vacancy centers in diamond," *Adv. Quantum Technol.* **3**, 1900069 (2020).
- <sup>79</sup>A. E. Rugar, S. Aghaeimebodi, D. Riedel, C. Dory, H. Lu, P. J. McQuade, Z.-X. Shen, N. A. Melosh, and J. Vučković, "Quantum photonic interface for tin-vacancy centers in diamond," *Phys. Rev. X* **11**, 031021 (2021).
- <sup>80</sup>D. Riedel, F. Fuchs, H. Kraus, S. Váth, A. Sperlich, V. Dyakonov, A. A. Soltamova, P. G. Baranov, V. A. Ilyin, and G. V. Astakhov, "Resonant addressing and manipulation of silicon vacancy qubits in silicon carbide," *Phys. Rev. Lett.* **109**, 226402 (2012).
- <sup>81</sup>S. E. Eonomou and P. Dev, "Spin-photon entanglement interfaces in silicon carbide defect centers," *Nanotechnology* **27**, 504001 (2016).
- <sup>82</sup>D. J. Christle, P. V. Klimov, C. F. de las Casas, K. Szász, V. Ivády, V. Jokubavicius, J. Ul Hassan, M. Syväjärvi, W. F. Koehl, T. Ohshima, N. T. Son, E. Jánzén, Á. Gali, and D. D. Awschalom, "Isolated spin qubits in SiC with a high-fidelity infrared spin-to-photon interface," *Phys. Rev. X* **7**, 021046 (2017).
- <sup>83</sup>C. P. Anderson, A. Bourassa, K. C. Miao, G. Wolfowicz, P. J. Mintun, A. L. Crook, H. Abe, J. Ul Hassan, N. T. Son, T. Ohshima, and D. D. Awschalom, "Electrical and optical control of single spins integrated in scalable semiconductor devices," *Science* **366**, 1225–1230 (2019).
- <sup>84</sup>D. M. Lukin, M. A. Guidry, and J. Vučković, "Integrated quantum photonics with silicon carbide: Challenges and prospects," *PRX Quantum* **1**, 020102 (2020).
- <sup>85</sup>T. Zhong, J. M. Kindem, J. G. Bartholomew, J. Rochman, I. Craiciu, E. Miyazono, M. Bettinelli, E. Cavalli, V. Verma, S. W. Nam, F. Marsili, M. D. Shaw, A. D. Beyer, and A. Faraon, "Nanophotonic rare-earth quantum memory with optically controlled retrieval," *Science* **357**, 1392–1395 (2017).
- <sup>86</sup>B. Casabone, J. Benedikter, T. Hümmer, F. Oehl, K. D. O. Lima, T. W. Hänsch, A. Ferrier, P. Goldner, H. de Riedmatten, and D. Hunger, "Cavity-enhanced spectroscopy of a few-ion ensemble in  $\text{Eu}^{3+}:\text{Y}_2\text{O}_3$ ," *New J. Phys.* **20**, 095006 (2018).
- <sup>87</sup>T. Zhong and P. Goldner, "Emerging rare-earth doped material platforms for quantum nanophotonics," *Nanophotonics* **8**, 2003–2015 (2019).
- <sup>88</sup>J. M. Kindem, A. Ruskuc, J. G. Bartholomew, J. Rochman, Y. Q. Huan, and A. Faraon, "Control and single-shot readout of an ion embedded in a nanophotonic cavity," *Nature* **580**, 201–204 (2020).
- <sup>89</sup>S. Chen, M. Raha, C. M. Phenicie, S. Ourari, and J. D. Thompson, "Parallel single-shot measurement and coherent control of solid-state spins below the diffraction limit," *Science* **370**, 592–595 (2020).
- <sup>90</sup>J. D. Caldwell, I. Aharonovich, G. Cassabo, J. H. Edgar, B. Gil, and D. N. Basov, "Photonics with hexagonal boron nitride," *Nat. Rev. Mater.* **4**, 552–567 (2019).
- <sup>91</sup>A. Dietrich, M. W. Doherty, I. Aharonovich, and A. Kubanek, "Solid-state single photon source with Fourier transform limited lines at room temperature," *Phys. Rev. B* **101**, 081401 (2020).
- <sup>92</sup>P. Maletinsky, S. Hong, M. S. Grinolds, B. Hausmann, M. D. Lukin, R. L. Walsworth, M. Loncar, and A. Yacoby, "A robust scanning diamond sensor for nanoscale imaging with single nitrogen-vacancy centres," *Nat. Nanotechnol.* **7**, 320–324 (2012).
- <sup>93</sup>M. Challier, S. Sonusen, A. Barfuss, D. Rohner, D. Riedel, J. Koelbl, M. Ganzhorn, P. Appel, P. Maletinsky, and E. Neu, "Advanced fabrication of single-crystal diamond membranes for quantum technologies," *Micromachines* **9**, 148 (2018).
- <sup>94</sup>L. Greuter, S. Starosielec, D. Najer, A. Ludwig, L. Duempelmann, D. Rohner, and R. J. Warburton, "A small mode volume tunable microcavity: Development and characterization," *Appl. Phys. Lett.* **105**, 121105 (2014).
- <sup>95</sup>C. Koks and M. P. van Exter, "Microcavity resonance condition, quality factor, and mode volume are determined by different penetration depths," *Opt. Express* **29**, 6879 (2021).
- <sup>96</sup>D. Riedel, Ph.D. thesis, University of Basel, Basel, 2017.
- <sup>97</sup>H. Kelkar, D. Wang, D. Martín-Cano, B. Hoffmann, S. Christiansen, S. Götzinger, and V. Sandoghdar, "Sensing nanoparticles with a cantilever-based scannable optical cavity of low finesse and sub- $\lambda^3$  volume," *Phys. Rev. Appl.* **4**, 054010 (2015).
- <sup>98</sup>J. F. S. Brachmann, H. Kaupp, T. W. Hänsch, and D. Hunger, "Photothermal effects in ultra-precisely stabilized tunable microcavities," *Opt. Express* **24**, 21205 (2016).
- <sup>99</sup>K. An, B. A. Sones, C. Fang-Yen, R. R. Dasari, and M. S. Feld, "Optical bistability induced by mirror absorption: Measurement of absorption coefficients at the sub-ppm level," *Opt. Lett.* **22**, 1433 (1997).
- <sup>100</sup>C. Santori, P. E. Barclay, K.-M. C. Fu, R. G. Beausoleil, S. Spillane, and M. Fisch, "Nanophotonics for quantum optics using nitrogen-vacancy centers in diamond," *Nanotechnology* **21**, 274008 (2010).
- <sup>101</sup>P. T. Kristensen, C. Van Vlack, and S. Hughes, "Generalized effective mode volume for leaky optical cavities," *Opt. Lett.* **37**, 1649 (2012).
- <sup>102</sup>J. Borregaard, A. S. Sørensen, and P. Lodahl, "Quantum networks with deterministic spin-photon interfaces," *Adv. Quantum Technol.* **2**, 1800091 (2019).
- <sup>103</sup>M. Ruf, N. H. Wan, H. Choi, D. Englund, and R. Hanson, "Quantum networks based on color centers in diamond," *J. Appl. Phys.* **130**, 070901 (2021).
- <sup>104</sup>T. D. Barrett, T. H. Doherty, and A. Kuhn, "Pushing Purcell enhancement beyond its limits," *New J. Phys.* **22**, 063013 (2020).
- <sup>105</sup>S. Häußler, J. Benedikter, K. Bray, B. Regan, A. Dietrich, J. Twamley, I. Aharonovich, D. Hunger, and A. Kubanek, "Diamond photonics platform based on silicon vacancy centers in a single-crystal diamond membrane and a fiber cavity," *Phys. Rev. B* **99**, 165310 (2019).